ORIGINAL ARTICLE

Open Access

Navigation performance analysis of Earth–Moon spacecraft using GNSS, INS, and star tracker

Dixing Wang[1,2], Tianhe Xu[1,2*] , Min Li[1,2] and Yali Shi[1,2]

Abstract

Global Navigation Satellite System (GNSS) can provide an approach for spacecraft autonomous navigation in earth–moon space to make up for the insufficiency of earth-based tracking, telemetry, and control systems. However, its weak power and poor observation geometry near the moon causes new problems. After the GNSS signal characteristics and satellite visibility were evaluated in Phasing Orbit and Lunar Transfer Orbit, we proposed an adaptive Kalman filter based on the Carrier-to-Noise ratio (C/N_0) and innovation vector to weaken the influence of GNSS accuracy attenuation as much as possible. The experimental results show that the spacecraft position and velocity accuracy are better than 10 m and 0.1 m/s near the Earth, and better than 50 m and approximately 0.2 m/s near the moon use GNSS with the proposed adaptive algorithms. Additionally, because of the deterioration of navigation performance based on the orbit filter during orbital maneuvering, we used accelerometer data to compensate for the dynamic model to maintain navigation performance. The results of the experiment provide a reference for subsequent studies.

Keywords Earth–moon spacecraft, Integrated navigation, Space service volume, Global navigation satellite system, Inertial navigation system, Star tracker

Introduction

Space research institutions worldwide have been investing significant energy into the moon, with numerous exploration missions planned to the moon as the destination. The 2018 and 2022 Global Exploration Roadmap supplement described the latest architecture for lunar surface missions, and contained a map of human mission planning for lunar exploration over the next decade (International Space Exploration Coordination Group, 2018, 2022). In recent years, notable lunar exploration missions have included the Chinese Chang'e—V,

American Artemis, and Japanese HAKUTO-R. Lunar exploration has emerged as the initial stride toward future human deep space exploration missions and will captivate the spotlight in the upcoming decade.

It is well known that the determination of the spacecraft position, velocity, and attitude is an important part of the exploration mission, and is currently the responsibility of the ground tracking, telemetry, and control group. The group forms a deep space network by building several monitoring stations on the ground, and uses the unified S-band system and very long baseline interferometry to determine the position and velocity of spacecraft (Erhu et al., 2023; Liu et al., 2022; Ulvestad, 1992). Although high-precision position and velocity can be obtained, the limitations of ground and on-board computing resources make it difficult to achieve the real-time tracking, telemetry, and control of large numbers of spacecraft. Therefore, spacecraft real-time autonomous

*Correspondence:
Tianhe Xu
thxu@sdu.edu.cn
[1] Institute of Space Science, Shandong University, No.180 Wenhua West Road, Huancui District, Weihai, Shandong Province, China
[2] Shandong Key Laboratory of Optical Astronomy and Solar-Terrestrial Environment, Weihai 264209, China

navigation has been a research direction with much attention (Ely et al., 2022).

Since the construction of the Global Navigation Satellite System (GNSS), many scholars have come to understand that it not only serves terrestrial users and Low Earth Orbit (LEO) satellites by using main lobe signals but also extends its service to Medium Earth Orbit (MEO), High Earth Orbit (HEO), and even ultra-HEO through its side lobe signals. The full Space Service Volume (SSV) of GNSS is shown in Fig. 1. The region from the Earth's surface to 3000 km altitude is usually called the Terrestrial Service Volume (TSV), the area from 3000 to 36,000 km is named SSV, and the area above 36,000 km is called Extended SSV (ESSV) (Bauer et al., 2017). In 2012, Work Group B (WG-B) of the International Committee on GNSS (ICG) identified the advantages of an interoperable GNSS SSV for the space user community. Subsequently, they have been working with GNSS service providers and space agencies to advance the SSV and consider its applications within and beyond cis-lunar space. Then WG-B officially released two booklets titled "The Interoperable Global Navigation Satellite Systems Space Service Volume" in 2018 and 2021, and the SSV characteristics of each constellation and service performance in space missions were analyzed (United Nations, 2021).

Other agencies and scholars have also focused on the performance of GNSS services in earth–moon space, and the characteristics and navigation performance of Global Position System (GPS) and Galileo satellite navigation system (Galileo) signals have been analyzed more deeply. The European Space Agency is interested in lunar exploration and motivated an experimental platform to evaluate the navigation performance of GPS L1C/A,

L5Q, Galileo E1C, and E5aQ signals in Lunar Transfer Orbit (LTO), Low Lunar Orbit (LLO), and descent and landing (D&L) in detail (Lopes et al., 2014). One of the most important points is satellite visibility, which needs to be modeled and simulated as accurately as possible. Shehaj et al. (2017) found that the Three-Dimensional (3D) GNSS antenna pattern model obviously affects satellite visibility in ultra-high orbit compared with the two-dimensional model. Accurate GPS and Galileo 3D antenna patterns were used to analyze the Carrier-to-Noise ratio (C/N_0), satellite availability, and Position Dilution of Precision (PDOP) of receivers in various orbits around the Moon. Delépaut et al. took into account the navigation message's C/N_0 demodulation threshold, and an "ephemeris-based visibility" approach was proposed to determine signal visibility (Delépaut et al., 2019, 2020). Also, some studies used GPS signals and inter-satellite links to determine the orbit and the time synchronization of the Lagrange orbit near the Moon, which verified the availability of GNSS in the global space of the Earth and moon (Iiyama et al., 2021; Qi & Oguri, 2023; Sirbu & Leonardi, 2023). As for BeiDou Navigation Satellite System (BDS), Lin et al. (2019) analyzed the propagation characteristics of the SSV signal in the ionosphere. Then Lin et al. (2020) used the 3D antenna pattern of BeiDou-3 Navigation Satellite System (BDS-3) satellites to simulate and analyze the Doppler shift, C/N_0, and measurement noise of the navigation signal for various space missions. The SSV service performance of BDS-3 and the advantages of Inclined Geo-Synchronous Orbit (IGSO) and Geostationary Orbit (GEO) satellites in SSV service were analyzed (Guan et al., 2022; Ma et al., 2023).

However, the performance of GNSS decreases with the distance from the Earth, so that it cannot provide high-precision navigation services for users in lunar space. Therefore, scholars have explored the integration of multi-sensors for more accurate spacecraft estimation state. Capuano et al. (2014) has been attempting to implement integrated navigation in ultra-high orbit since 2014, and proposed the integration of the Inertial Navigation System (INS), GNSS, star tracker, and orbital filter to obtain higher precision and robust navigation performance. An autonomous navigation system was designed and used to provide real-time autonomous navigation and attitude determination for LEO, GEO, and even higher HEO missions (Capuano et al., 2017, 2018). However, accelerometers can only measure non-gravitational forces in space and cannot provide a complete dynamic model for spacecraft (Wei et al., 2023), some conclusions may need to be refined more clearly.

As a common attitude determination sensor, star tracker can provide a high-precision attitude for the vehicle. Therefore, some multi-sensors integration methods
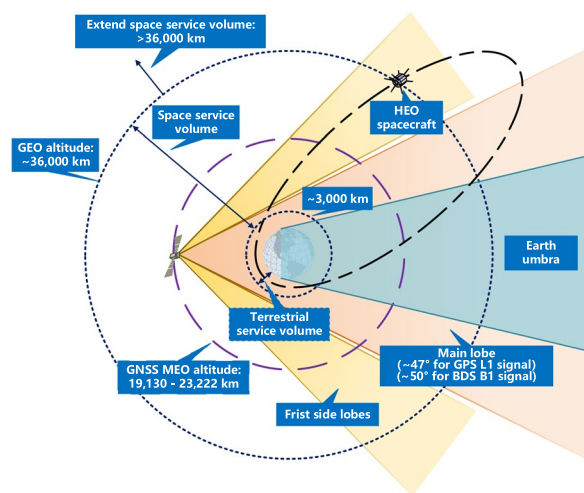

Fig. 1 Signal reception geometry in the space service volume

Wang *et al. Satellite Navigation*   (2024) 5:16

Page 3 of 22

and adaptive algorithms have been proposed, including decentralized data fusion methods such as federated filtering, in addition to centralized extended Kalman filtering (Gao et al., 1993). At present, it widely integrated with INS and GNSS to provide autonomous navigation services for ground and near-earth vehicles, even include lunar and Mars surface probes (Gao et al., 2018; Hu et al., 2023; Ning et al., 2011). Different from the general scenario, star tracker is more commonly integrated with an Earth sensor and orbital filter to provide the position and velocity for spacecraft (called starlight angle navigation), in addition to providing the spacecraft with a high-precision attitude, and is widely used in deep space probes because of its autonomy (Bhaskaran et al., 2000; Yu et al., 2021). However, it is limited by the performance of the Earth sensor, which results in low navigation performance. Many scholars have attempted to improve navigation accuracy by combining laser ranging, accelerometer, and other methods (Gui et al., 2021; Li et al., 2022a; Wang & Zhang, 2013). With the improvement of the accuracy of the earth sensor, the integration of starlight angle navigation and GNSS will be the main autonomous navigation method for the future Earth–moon space spacecraft and requires further study.

After studying various difficulties in the autonomous navigation of earth–moon spacecraft, we believe that the primary problem for GNSS is to overcome precision attenuation as the distance increases. Additionally, the spacecraft will suffer from inevitable dynamic disturbance, such as orbital maneuver, descent, and landing, which will also cause a significant decline in navigation performance.

To solve these problems, we first simulate the observations of the GNSS receiver, IMU, and star tracker based on the Phasing Orbit (PHO) and LTO of the lunar probe,

and analyze the signal characteristics and visibility of GPS and BDS in earth–moon space. Then we propose an adaptive algorithm based on the innovation vector to reflect the change of observation noise more accurately to suppress the precision attenuation of GNSS near the moon and improve spacecraft navigation performance. Finally, we use accelerometers during orbital maneuvers to compensate for the dynamic model, and integrate INS, GNSS, and star tracker to maintain navigation performance.

This paper is structured as follows: the models and algorithms were described for the adaptive Kalman filter in detail in "Models and algorithms" section. Then the modeling and simulation approach for the sensors were introduced in "Observation simulation and characteristic analysis" section. Finally, we analyze the solution results of various schemes used to evaluate the proposed approaches in "Experiments and analysis" section. And the conclusions and discussions are drawn in "Conclusions and discussion" section.

Models and algorithms

First, to respond to the various states of earth–moon spacecraft, an autonomous navigation method based on orbital dynamics, assisted by GNSS, INS, and star tracker, is shown Fig. 2. Given the clear understanding of orbital dynamics, we use GNSS based on orbital filtering as the primary navigation method. Considering the on-board accelerometer can only measure non-gravitational acceleration so that the non-gravitational model can be replaced by accelerometer data. We only use the accelerometer observations when the spacecraft is subjected to additional and unmodeled non-gravitational accelerations acceleration (e.g., the thrust of the thruster).
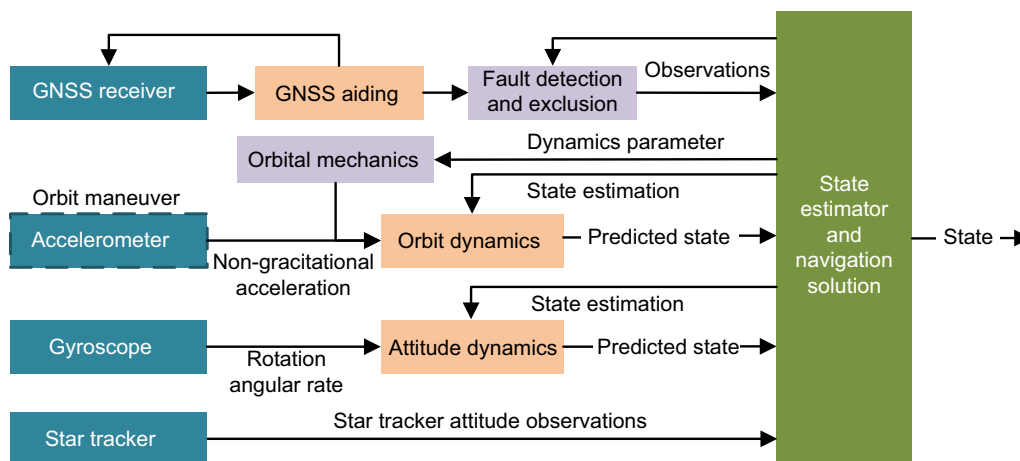
Fig. 2 Preliminary architecture of the integrated navigation system

Wang *et al. Satellite Navigation* (2024) 5:16

Page 4 of 22

Regarding the star tracker, we only use it as an attitude determination system in our experiments.

Setting of the Kalman filter

For nonlinear stochastic model, the dynamic model and measurement model are shown in Eq. (1) and (2) as follow:

$$X_k = f\{X_{k-1}\} + w_k \tag{1}$$

$$z_k = h\{X_k\} + v_k \tag{2}$$

where X_k is the state parameter at epoch k; z_k is measurement vector at epoch k; $f\{\cdot\}$ is nonlinear dynamic state function and $h\{\cdot\}$ represents nonlinear measurement function. Both w_k and v_k are modeled as zero-mean Gaussian white noise in dynamic model and measurement model, with process noise covariance matrix Q_k and measurement noise covariance matrix R_k. Moreover, the assumption is that w_k and v_k remain uncorrelated with each other at any time, which can be expressed as

$$\begin{array}{c} E(w_k) = 0 \quad D(w_k) = Q_k \delta_{k,k-1} \\ E(v_k) = 0 \quad D(v_k) = R_k \delta_{k,k-1} \\ D(w_k, v_k) = 0 \end{array} \tag{3}$$

where $E(\cdot)$ is defined as expectation operation, and $D(\cdot)$ is defined as covariance operation.

After linearization, the dynamic model and observation model can be expressed as:

$$x_k = \boldsymbol{\Phi}_{k,k-1} x_{k-1} + w_k \tag{4}$$

$$z_k = H_k x_k + v_k \tag{5}$$

where $\boldsymbol{\Phi}_{k,k-1}$ is called the state transition matrix from epoch k–1 to k; H_k denotes the measurement matrix.

For conventional orbital filtering, the unknown state parameters X_k of the k-th epoch can be expressed as

$$X_k = \begin{bmatrix} \vec{r} & \vec{v} & C_R & c \cdot \mathrm{d}t \end{bmatrix}^{\mathrm{T}}_{8 \times 1} \tag{6}$$

which comprises the 3D position and velocity vectors $\vec{r}$ and $\vec{v}$ in Earth-centered inertial reference frame (*i*-frame); one solar radiation pressure coefficient C_R; the receiver clock offset parament dt in seconds (Li et al., 2022b); and the speed of light c.

The state transfer matrix can be calculated using the orbit dynamic model:

$$\boldsymbol{\Phi}_{k,k-1} = \begin{bmatrix} \boldsymbol{\varphi}_x & \boldsymbol{\varphi}_{C_R} & 0 \\ 0 & I & 0 \\ 0 & 0 & I \end{bmatrix}_{8 \times 8} \tag{7}$$

where $\boldsymbol{\varphi}_x = \begin{bmatrix} \partial\vec{r}/\partial\vec{r} & \partial\vec{r}/\partial\vec{v} \\ \partial\vec{v}/\partial\vec{r} & \partial\vec{v}/\partial\vec{v} \end{bmatrix}_{6 \times 6}$ and $\boldsymbol{\varphi}_{C_R} = \begin{bmatrix} \partial\vec{r}/\partial C_R \\ \partial\vec{v}/\partial C_R \end{bmatrix}_{6 \times 1}$ is the state transition matrixes of orbital dynamics; Δt is the time interval and I is a unit matrix.

As mentioned above, on-board accelerometers have sufficient accuracy but only can measure non-gravitational acceleration. The forces on the spacecraft during orbital maneuvers can be expressed as

$$\vec{F}_{\mathrm{all}} = \vec{F}_G + \vec{F}_{\mathrm{NG}} = \left(\vec{F}_{\mathrm{earth}} + \vec{F}_{\mathrm{sun}} + \vec{F}_{\mathrm{moon}} + \vec{F}_n \right) + \left(\vec{F}_{\mathrm{srp}} + \vec{F}_{\mathrm{man}} + \vec{F}_\varepsilon \right) \tag{8}$$

The gravitational force $\vec{F}_G$ include the Earth's gravity $\vec{F}_{\mathrm{earth}}$, Sun's gravity $\vec{F}_{\mathrm{sun}}$, moon's gravity $\vec{F}_{\mathrm{moon}}$, and gravity of other celestial bodies $\vec{F}_n$. The non-gravitational force $\vec{F}_{\mathrm{NG}}$ mainly includes solar radiation pressure $\vec{F}_{\mathrm{srp}}$, thruster thrust $\vec{F}_{\mathrm{man}}$, and other unmodeled forces $\vec{F}_\varepsilon$. The maneuvering time is usually short and the gravitational force is relatively stable, whereas the non-gravitational force can be measured by the accelerometer. Therefore, the pseudo-observations of IMU can be constructed and the spacecraft state during orbital maneuvering can be estimated using the integrated navigation system.

In general, the on-board accelerometer is installed parallel to the spacecraft body frame (*b*-frame), and the non-gravitational force $\vec{F}_{\mathrm{NG}}$ under the *i*-frame can be expressed as

$$\vec{F}_{\mathrm{NG}} = \vec{F}_{\mathrm{srp}} + \vec{F}_{\mathrm{man}} + \vec{F}_\varepsilon = C_b^i \vec{F}_{\mathrm{NG},b} \tag{9}$$

where C_b^i is the rotation matrix from *b*-frame to *i*-frame, which can be obtained from the spacecraft attitude. The dynamic equation of INS in the *i*-frame can be described as

$$\begin{bmatrix} \vec{r} \\ \vec{v} \\ C_b^i \end{bmatrix}_{k+1} = \begin{bmatrix} \vec{v} \\ C_b^i \vec{f}_{ib}^b + \vec{F}_G \\ C_b^i \boldsymbol{\Omega}_{ib}^b \end{bmatrix}_k \tag{10}$$

where $\vec{r}$ and $\vec{v}$ denote position and velocity vectors in the *i*-frame, respectively; $\vec{f}_{ib}^b$ is the specific force vector in the *b*-frame; $\vec{F}_G$ is the gravitational forces in the *i*-frame which is related to the position $\vec{r}$ and can be obtained by precise dynamic model. $\boldsymbol{\Omega}_{ib}^b$ is the skew-symmetric matrix of $\boldsymbol{\omega}_{ib}^b$, while $\boldsymbol{\omega}_{ib}^b$ is the rotation angular rate of gyroscopes output.

Usually, in order to suppress the error dispersion of INS, in addition to integrating with GNSS, it is also integrated with star tracker to form an INS, GNSS and Star tracker integrate navigation system. And the accurate position, velocity and attitude can also be obtained even if the dynamic model provided by orbital mechanics is

inaccurate. The parameters to be estimated for the integration system can be expressed as

$$X_k = \left[\vec{r} \ \vec{v} \ \vec{\psi} \ \vec{b}_a \ \vec{b}_g \ c \cdot \mathrm{d}t \right]^{\mathrm{T}}_{16 \times 1} \qquad (11)$$

where, in addition to 3D position vector $\vec{r}$, velocity vector $\vec{v}$, receiver clock offset $\mathrm{d}t$; additional parameters include spacecraft 3D attitude $\vec{\psi}$, the accelerometer bias $\vec{b}_a$ and gyros bias $\vec{b}_g$.

The state transition matrix $\boldsymbol{\Phi}^{\mathrm{INS}}_{k,k-1}$ of the INS in the i-frame can be expressed as

$$\boldsymbol{\Phi}^{\mathrm{INS}}_{k,k-1} = \begin{bmatrix} 0_3 & \boldsymbol{I}_3 & 0_3 & 0_3 & 0_3 & 0 \\ \boldsymbol{N}_g & 0_3 & \left(\boldsymbol{C}^i_b \cdot \vec{f}^b_{ib} \right) \wedge & \boldsymbol{C}^i_b & 0_3 & 0 \\ 0_3 & 0_3 & \boldsymbol{\omega}^b_{ib} & 0_3 & -\boldsymbol{C}^i_b & 0 \\ 0_3 & 0_3 & 0_3 & 0_3 & 0_3 & 0 \\ 0_3 & 0_3 & 0_3 & 0_3 & 0_3 & 0 \\ 0 & 0 & 0 & 0 & 0 & \boldsymbol{I} \end{bmatrix}_{16 \times 16} \qquad (12)$$

where $\boldsymbol{N}_g = \partial \vec{F}_g / \partial \vec{r}$, $\wedge$ is the symbol for calculate the skew-symmetric matrix, $\boldsymbol{I}_3$ is a 3-order unit matrix and 0_3 is a 3-order zero matrix.

After we get the state transfer matrix for orbital filtering $\boldsymbol{\Phi}_{k,k-1}$ and that for INS $\boldsymbol{\Phi}^{\mathrm{INS}}_{k,k-1}$, respectively, the predicted state $\tilde{X}_k$, covariance matrix $\tilde{P}_k$, and epoch time k can be expressed as

$$\tilde{X}_k = \boldsymbol{\Phi}_{k,k-1} \overline{X}_{k-1} \qquad (13)$$

$$\tilde{P}_k = \boldsymbol{\Phi}_{k,k-1} \overline{P}_{k-1} \boldsymbol{\Phi}^{\mathrm{T}}_{k,k-1} + \boldsymbol{Q}_k \qquad (14)$$

where $\overline{X}_{k-1}$ and $\overline{P}_{k-1}$ are the estimated state and corresponding covariance matrix, respectively. $\boldsymbol{Q}_k$ is the covariance matrix of system noise and represents the accuracy of the dynamic model.

As for the orbit filter, the pseudo-range ρ of GNSS as the observation, if n satellites are observed at epoch time k, the measurement matrix $\boldsymbol{H}_k$, and measurement innovation δz_k can be expressed as

$$\boldsymbol{H}_k = \begin{bmatrix} \boldsymbol{e}_1 & 0_3 & 0 & 1 \\ \boldsymbol{e}_2 & 0_3 & 0 & 1 \\ \vdots & \vdots & \vdots & \vdots \\ \boldsymbol{e}_n & 0_3 & 0 & 1 \end{bmatrix}_{n \times 8} \qquad (15)$$

and

$$\delta z_k = z_k - \boldsymbol{H}_k \tilde{X}_k = \begin{bmatrix} \hat{\rho}_1 - \tilde{\rho}_1 \\ \hat{\rho}_2 - \tilde{\rho}_2 \\ \vdots \\ \hat{\rho}_n - \tilde{\rho}_n \end{bmatrix}_{n \times 1} \qquad (16)$$

where the predicted value and measured value of $*$ are represented by $\tilde{*}$ and $\hat{*}$, respectively. $\boldsymbol{e}_i$ is the unit vector of the line-of-sight direction from the GNSS receiver to the i-th satellite. z_k is the observation at epoch time k.

As for INS, GNSS and Star tracker integrate navigation system, if m observations of the Star tracker also be considered, the measurement matrix and measurement innovation can be rewritten as

$$\boldsymbol{H}_k = \begin{bmatrix} \boldsymbol{e}_1 & 0_3 & 0_3 & 0 & 1 \\ \vdots & \vdots & \vdots & \vdots & \vdots \\ \boldsymbol{e}_i & 0_3 & 0_3 & 0 & 1 \\ 0_3 & 0_3 & \boldsymbol{u}_1 & 0 & 1 \\ \vdots & \vdots & \vdots & \vdots & \vdots \\ 0_3 & 0_3 & \boldsymbol{u}_i & 0 & 1 \end{bmatrix}_{(n+3m) \times 16} \qquad (17)$$

and

$$\delta z_k = z_k - \boldsymbol{H}_k \tilde{X}_k = \begin{bmatrix} \hat{\rho}_i - \tilde{\rho}_i \\ \vdots \\ \hat{\vec{l}}_j - \tilde{\vec{l}}_j \end{bmatrix}_{(n+3m) \times 1} \qquad (18)$$

where $\vec{l}_j$ is the unit vector of the j-th star in the b-frame; $\hat{\vec{l}}_j = \boldsymbol{C}^b_i \vec{r}^S_j$, $\boldsymbol{C}^b_i$ is the inverse matrix of $\boldsymbol{C}^i_b$, and $\vec{r}^S_j$ is the unit vector of the j-th star in the i-frame.

In addition, according to Eq. (10), the attitude dynamics does not depend on other parameters except rotation angular rate, so the attitude of the spacecraft can be independently calculated according to the outputs of the gyroscope and the star tracker.

Then the measurement is updated, and gain matrix $\boldsymbol{K}_k$, estimated state $\overline{X}_k$, and covariance matrix $\overline{P}_k$ can be calculated using

$$\boldsymbol{K}_k = \tilde{P}_k \boldsymbol{H}^{\mathrm{T}}_k \left(\boldsymbol{H}_k \tilde{P}_k \boldsymbol{H}^{\mathrm{T}}_k + \boldsymbol{R}_k \right)^{-1} \qquad (19)$$

$$\overline{X}_k = \tilde{X}_k + \boldsymbol{K}_k \delta z_k \qquad (20)$$

$$\overline{P}_k = (\boldsymbol{I} - \boldsymbol{K}_k \boldsymbol{H}_k) \tilde{P}_k \qquad (21)$$

where gain matrix $\boldsymbol{K}_k$ determines the weight of observation information when the state is updated. $\boldsymbol{R}_k$ is the covariance matrix of observation noise and is a diagonal matrix composed of independent observation variance σ^2 at epoch time k. If observation noise increases, it is necessary to reduce the weight of observation information by adjusting the $\boldsymbol{R}$ matrix and reducing matrix $\boldsymbol{K}_k$.

GNSS fault detection and exclusion base on integrated system

As we all know, GNSS observations will inevitably have failures in practical situation, especially in the environment of weak signals in deep space, will make the wrong state parameters output by the estimator and reduce the accuracy of autonomous navigation. Therefore, Fault Detection and Exclusion (FDE) must be applied before the integrated solution.

In the Kalman filtering of integrated system, the predicted state $\tilde{X}_k$ and measurement vector z_k are integrated. The unknown parameters are estimated through the least squares estimation, and the measurement model is given by (Aghapour & Farrell, 2019; Hewitson & Wang, 2007; Jiang et al., 2020):

$$L_k = A_k Y_k + V_k \tag{22}$$

where A_k denotes the design matrix, V_k denotes the residual vector, and

$$L_k = \begin{bmatrix} z_k; \tilde{X}_k \end{bmatrix} \tag{23}$$

$$A_k = [H_k; I] \tag{24}$$

$$V_k = \begin{bmatrix} V_{z_k}; V_{\tilde{X}_K} \end{bmatrix} \tag{25}$$

$$C_{L_k} = \begin{bmatrix} R_k & 0 \\ 0 & P_k^- \end{bmatrix} \tag{26}$$

where V_{z_k} denotes the residual vector of the measurement, $V_{\tilde{X}_K}$ denotes the residual vector of the predicted state, C_{L_k} denotes the covariance matrix corresponding to the measurement model (Hewitson & Wang, 2007). Based on the least squares estimation, the estimation of state parameters $\tilde{Y}_k$ and its covariance matrix $Q_{\tilde{X}_K}$ are obtained by

$$\tilde{Y}_k = \left(A_k^{\mathrm{T}} C_{L_k}^{-1} A_k \right)^{-1} A_k^{\mathrm{T}} C_{L_k}^{-1} L_k \tag{27}$$

$$Q_{\tilde{Y}_k} = \left(A_k^{\mathrm{T}} C_{L_k}^{-1} A_k \right)^{-1} \tag{28}$$

Residual vector of the measurements V_k and its covariance matrix Q_{V_k} are derived by:

$$V_k = A_k \tilde{Y}_k - L_k \tag{29}$$

$$Q_{V_k} = C_{L_k} - A_k Q_{\tilde{Y}_k} A_k^{\mathrm{T}} \tag{30}$$

In the integrated navigation system, the test statistics λ_k is defined based on the residual and its covariance matrix, namely,

$$\lambda_k = V_k^{\mathrm{T}} C_{L_k}^{-1} V_k \tag{31}$$

λ_k obeys the Chi-square distribution with the freedom degree of $m−n$, namely,

$$\chi_{m-n}^2(1 - \alpha/2) \leq \lambda_k \leq \chi_{m-n}^2(\alpha/2) \tag{32}$$

where m is number of observations and n is number of unknown state parameters. It indicates no failures if the statistics satisfy the Eq. (32), once λ_k is bigger than $\chi_{m-n}^2(\alpha)$, the fault is detected.

After the failure identification is applied to locate failure and a fault has been detected with the global detection algorithm, the ω-test can then be used to identify the corresponding measurement (Teunissen, 1998), where the test statistic is defined as

$$\omega_i = \left| e_i^{\mathrm{T}} C_{L_k} V_k / \sqrt{e_i^{\mathrm{T}} C_{L_k} Q_{V_k} C_{L_k} e_i} \right| \tag{33}$$

where, $e_i = \begin{bmatrix} 0 & \cdots & 1 & \cdots & 0 \end{bmatrix}^{\mathrm{T}}$ is a zero vector whose i-th element is set to 1. ω_i obeys the normal distribution when no failures exist, namely, $\omega_i \sim N(0, 1)$. In the presence of outliers, the test statistics would be bigger than the threshold $T_D = N_{\alpha/2}(0, 1)$ (α here is set to 0.1%, and the corresponding threshold $T_D = 3.2905$), and the i-th measurement is thought failure. Accordingly, the failure identification is completed.

Adaptive estimation algorithm

As mentioned above, the real noise v of the observation is difficult to obtain; hence, matrix R is generally set to an empirical constant. However, different from the ground environment, when a spacecraft flies away from the Earth, the measurement noise of the GNSS signal increases significantly because of the free space propagation loss and the positioning geometry becomes worse inevitably. Therefore, noise covariance matrix R needs to be adjusted adaptively to the approximate actual measurement noise. In this section, we introduce two adaptive estimation algorithms: "Measurement Noise-Based Adaptive Estimation" (MBAE) and "Innovation-Based Adaptive Estimation" (IBAE).

MBAE

The measurement noise is mainly caused by sign free space loss in deep space. So that in addition to setting the initial measurement noise, we also use a formula related to C/N_0 in every epoch to make the noise covariance matrix approach the actual measurement noise more

accurately. The covariance matrix of the measurements can be given by

$$\boldsymbol{R}_k^{\mathrm{MBAE}} = \begin{bmatrix} m\sigma_{\rho_1}^2 & \cdots & 0 \\ \vdots & \ddots & \vdots \\ 0 & \cdots & m\sigma_{\rho_n}^2 \end{bmatrix}_{n \times n} \tag{34}$$

where $\sigma_{\rho_i k}$ is the pseudo-range measurement noise of the i-th satellite, and is set to 10 m. The coefficient m can be calculated using a modified sigma-Δ model and calculated from the receiver C/N_0 (Brunner et al., 1999), which can be described as

$$m = a + b \cdot 10^{-\frac{C/N_0}{10}} \tag{35}$$

where the coefficients a and b are obtained using a priori fitting based on different navigation systems and different frequencies. Using the above equations, the adaptive estimation of the measurement noise matrix at low C/N_0 can be achieved, which results in an approximation of the actual measurement noise.

IBAE

Based on the MBAE algorithm above, we can obtain the covariance matrix of the theoretical measurement noise. However, obviously, the actual measurement noise is caused by various factors, such as multipath effects, in addition to signal free space loss, Eq. (35) cannot fully represent the real measurement noise. Therefore, additional algorithms are needed to further improve the navigation accuracy with weak signals.

When the dynamic model is accurate and observation noise increases, the measurement innovation δz_k obviously increases, which is the difference between the observation value z_k and predicted value $H_k \tilde{X}_k$. According to this characteristic, we construct an adaptive algorithm based on measuring innovation.

According to Eq. (3) and (5), Eq. (3) can be rewritten as

$$E\left[(z_k - H_k X_k)(z_k - H_k X_k)^{\mathrm{T}}\right] = 0 \tag{36}$$

$$D\left[(z_k - H_k X_k)(z_k - H_k X_k)^{\mathrm{T}}\right] = \boldsymbol{R}_k \tag{37}$$

In addition, covariance matrix $\tilde{\boldsymbol{P}}_k$ in the Kalman filter is the mathematical covariance of the difference between predicted state $\tilde{X}_k$ and truth value X_k, which can be expressed as

$$D\left[\left(\tilde{X}_k - X_k\right)\left(\tilde{X}_k - X_k\right)^{\mathrm{T}}\right] = \tilde{\boldsymbol{P}}_k \tag{38}$$

Therefore, the squared uncertainty of the vector $H_k \tilde{X}_k$ predicted by the predicted state $\tilde{X}_k$ is

$$D\left[\left(H_k \tilde{X}_k - H_k X_k\right)\left(H_k \tilde{X}_k - H_k X_k\right)^{\mathrm{T}}\right] = H_k \tilde{\boldsymbol{P}}_k H_k^{\mathrm{T}} \tag{39}$$

Consequently, according to Eq. (16), The mathematical expectation and covariance of the measurement innovation δz_k can be expressed as

$$E\left[\delta z_k \delta z_k^{\mathrm{T}}\right] = 0 \tag{40}$$

$$D\left[\delta z_k \delta z_k^{\mathrm{T}}\right] = H_k \tilde{\boldsymbol{P}}_k H_k^{\mathrm{T}} + \boldsymbol{R}_k \tag{41}$$

So far, we can find that the measurement innovation δz_k obeys a Gaussian normal distribution with a mean of zero and a variance of $H_k \tilde{\boldsymbol{P}}_k H_k^{\mathrm{T}} + \boldsymbol{R}_k$, i.e., $\delta z_k \sim N(0, H_k \tilde{\boldsymbol{P}}_k H_k^{\mathrm{T}} + \boldsymbol{R}_k)$.

Generally, in the process of state estimation using Kalman filter, if the variance $\boldsymbol{R}_{k+1}$ of noise w_{k+1} increases for the measurement z_{k+1} at epoch time $k+1$ and the dynamic model is accurate and stable, the variance $H_{k+1} \tilde{\boldsymbol{P}}_{k+1} H_{k+1}^{\mathrm{T}} + \boldsymbol{R}_{k+1}$ of the measurement innovation δz_k will also increase. In this case, it is necessary to use the variance expansion method to reduce the weight of observation information in the state update.

According to Eq. (36) and (37), a standardized innovation vector $\tilde{S}_{\delta z,k}$ at epoch k can be defined as follows

$$\tilde{S}_{\delta z,k} = \frac{\delta z_k}{\sqrt{H_k \tilde{\boldsymbol{P}}_k H_k^{\mathrm{T}} + \boldsymbol{R}_k}} \tag{42}$$

where the standardized innovation vector $\tilde{S}_{\delta z,k}$ obeys the normal distribution when the covariance $\boldsymbol{R}_k$ can be given accurately. It is obviously impossible and is set to an empirical constant in the case of high quality and stable observations. But it cannot be applied to deep space environments with weak signals.

Therefore, the sigma-Δ model is used to obtained the prior covariance matrix $\boldsymbol{R}_k^{\mathrm{MBAE}}$, which is more accuracy than the empirical constant. Then the covariance matrix $\boldsymbol{R}_k$ in Eq. (42) can be rewritten as $\boldsymbol{R}_k^{\mathrm{MBAE}}$.

We can see that the standardized innovation vector can reflect the change of observation noise. Therefore, adaptive factor ω_k can be constructed and the observation noise covariance matrix $\boldsymbol{R}_k^{\mathrm{MBAE}}$ of the k-th epoch can be reconstructed as $\tilde{\boldsymbol{R}}_k$. The calculation method for adaptive factor ω_k and the reconstruction method for the measurement noise covariance matrix, respectively, are given as follows:

Wang *et al. Satellite Navigation*　　(2024) 5:16

Page 8 of 22

$$\omega_k = \begin{cases} 1 & \left|\tilde{\boldsymbol{S}}_{\delta z,k}\right| \le k_0 \\ \dfrac{k_0}{\left|\tilde{\boldsymbol{S}}_{\delta z,k}\right|} \times \left(\dfrac{k_1 - \left|\tilde{\boldsymbol{S}}_{\delta z,k}\right|}{k_1 - k_0}\right) & k_0 < \left|\tilde{\boldsymbol{S}}_{\delta z,k}\right| \le k_1 \\ 0 & \left|\tilde{\boldsymbol{S}}_{\delta z,k}\right| > k_1 \end{cases} \quad (43)$$

$$\tilde{\boldsymbol{R}}_k = \omega_k^{-1} \boldsymbol{R}_k^{\text{MBAE}} \quad (44)$$

where k_0 and k_1 are two empirical constants, which are usually selected in the ranges of 2.0–3.0 and 4.5–8.5, respectively (Yang et al., 2010). In this paper, we set the values to 2 and 7.5, respectively. Equation (42) shows that when innovation vector δz_k is small, the quality of observations is relatively stable; and an increase in vector δz_k means that the noise of the observation increases, which results in the increase of the vector $\tilde{\boldsymbol{S}}_{\delta z,k}$. At this time the adaptive factor ω_k need to be used to expand covariance matrix $\boldsymbol{R}_k^{\text{MBAE}}$, and reduce the weight of observation in the state update. However, when observation noise is too large, the weight of observation needs to be minimized. The covariance matrix $\tilde{\boldsymbol{R}}_k$ obtained by the above method is substituted into Eq. (19) for subsequent measurement updates to obtain estimated parameters.

The IBAE algorithm can adaptively estimate the measurement noise covariance matrix according to the measurement innovation, which is suitable for earth–moon space, where GNSS measurement noise changes greatly; however, the initial value must be as accurate as possible. Hence, it is necessary to use the MBAE algorithm to determine the noise covariance matrix before the IBAE algorithm is applied. The adaptive Kalman filter solving process with the FDE, IBAE and MBAE algorithms is shown in Fig. 3.

We used simulation data to verify the effectiveness of above algorithms. In "Observation simulation and characteristic analysis" section, we focus on the simulation of observed data from multiple sensors and the GNSS signal characteristics was also analyzed. The navigation performance of earth–moon spacecraft was analyzed with the simulated observations and the adaptive algorithms in "Experiments and analysis" section.

Observation simulation and characteristic analysis
Parameters of the simulation orbit
We consider a typical earth–moon space exploration project: "Chang'e-I" (named as CE-1) as an example. As shown in Fig. 4, the orbit of the CE-1 spacecraft consists
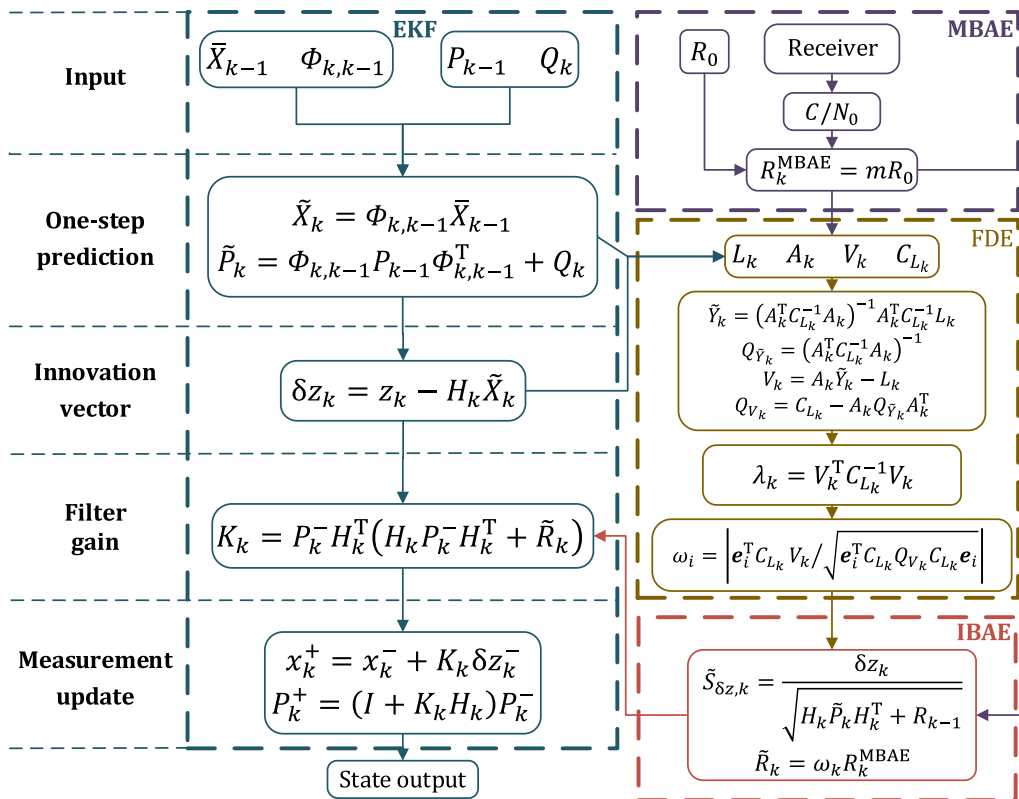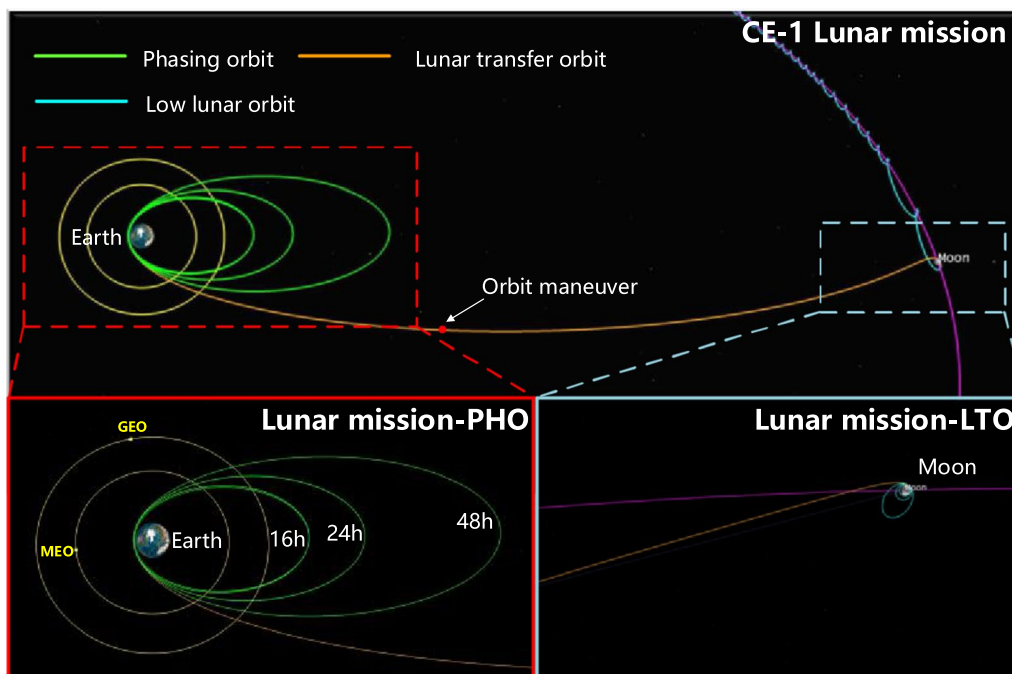

Fig. 3 Adaptive Kalman filtering algorithm procedure

Fig. 4 CE-1 lunar mission trajectory: the green and orange trajectories are PHO and LTO, respectively, and the yellow trajectory represents GNSS MEO and GEO. The orbit maneuver point is also marked

Table 1 Initial state parameter settings for the simulation orbits

Orbit	Orbital period (h)	Initial epoch [MJD]		Initial State in ECI
PHO	48	54,211.952688	Pos (m)	6,965,138.922, 57,315.612, 1581.364
			Vel (m/s)	− 72.280, 8931.660, − 5363.521
LTO	96	54,213.945739	Pos (m)	2,405,932.950, − 5,294,449.058, − 3,021,365.507
			Vel (m/s)	10,190.645, 3593.586, 1722.103

of PHO and LTO. PHO includes multiple HEOs with 16-h, 24-h, and 48-h periods. The spacecraft makes several adjustments in PHO before entering LTO and finally reaching the Moon. The 48-h PHO and LTO for the data simulation and analysis were selected and the detailed initial state parameters and dynamic model settings used in the simulation are shown in Tables 1 and 2, respectively.

We simulated the spacecraft attitude using "Satellite Tool Kit" software and set the attitude mode to "Nadir alignment with ECI velocity constraint." The body Z axis points towards the nadir, and the X axis is constrained by the direction of inertial velocity. Then the observations from multi-sensors can be simulated.

GNSS
Celestial eclipse and signal propagation loss are the main factors that affect satellite visibility and the signal measurement accuracy of deep space GNSS receivers.

Table 2 Dynamic parameter settings for the simulation orbits

Dynamic model	Setting
Earth gravity model	EIGEN-6C(70×70) (Förste et al., 2012)
Moon gravity model	GL0660B(30×30) (Konopliv et al., 2013)
N-body	JPL DE405
Solar radiation pressure	Macro model (Montenbruck & Gill, 2012) Mass:1000 kg, Area: 26.78 m², C_R = 1.24
Solid tide and pole tide	IERS 2010 (Petit & Luzum, 2010)
Ocean tide	FES 2004 (Lyard et al., 2006)
Relatively	IERS 2010

Obviously, the main eclipse body for PHO and LTO in earth–moon space is the Earth, and for LLO and D&L, the Moon is also included.

We use the geometric approach to determine whether the satellite signal is blocked by the Earth. As shown in Fig. 5, θ_{main} is the threshold of the available range of the
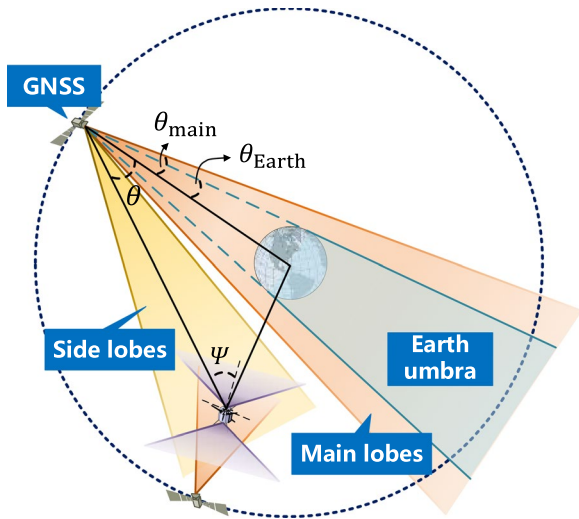
Fig. 5 Geometry between GNSS satellites, spacecraft, and the Earth: spacecraft can receive GNSS signals from both the zenith and nadir directions

Table 3 Earth eclipse angle and main lobe angle of BDS-3 and GPS

Navigation system	BDS-3		GPS
	MEO	**GEO/IGSO**	**MEO**
eclipse angle (°)	13.21	8.7	13.84
main lobe angle (°)	25.0	19.0	26.0

GNSS main lobe signal, beyond which the side lobe signal is considered to be received. Ψ is the off-boresight angle of the receiver antenna, which is related to the receiver antenna gain. Additionally, eclipse angle θ_{Earth} is also defined, and the spacecraft-satellite-Earth angle is marked as θ. According to geometry, satellite visibility and the type of signal received can be determined.

The earth eclipse angle and main lobe angle of BDS-3 and GPS are shown in Table 3 (Rathinam & Dempster, 2016).

Signal propagation loss and receiver receiving power are key parameters in the simulation. We choose BDS-3 B1C and GPS L1 as the frequency of simulated observations. The simulation parameter settings of the observations are shown in Table 4.

The simulation methods to calculate the C/N_0 of the GNSS receiver is shown below:

$$C/N_0 = P_T + G_T + G_R + L_S - L_A - N_0 \tag{45}$$

where P_T is the output power of the transmitter amplifier; G_T is the transmitter antenna gain, which relates to the elevation and azimuth; G_R is the receiver antenna gain, which relates to the off-boresight angle; and L_S represents the free space propagation loss. L_A is the influence of the atmosphere and we set it to 0 dB Hz in our simulation because of the small influence. N_0 is the noise power spectrum density and can be calculated as

$$N_0 = 10 lg k T_s \tag{46}$$

where $k = 1.3806505 \times 10^{-23}$ J/K is the Boltzmann constant and T_s is the system noise temperature.

After we obtain the receiver C/N_0 using Eq. (45), the theoretical code noise can be calculated according to the signal modulation method. For GPS L1 signals using Binary Phase Shift Keying (BPSK) modulation, thermal noise code tracking jitter σ_{DLL} can be calculated as

$$\sigma_{DLL} \cong \sqrt{\frac{B_n}{2 \cdot C/N_0} D \left[1 + \frac{2}{T \cdot C/N_0 (2-D)} \right]} \tag{47}$$

where $B_n = 0.05$ is the code loop noise bandwidth in Hz, $D = 0.25$ is the early-to-late correlator spacing in chips. $T = 0.02$ is the coherent integration time in seconds.

Table 4 Parameter settings for the simulation observations

Item	Setting
Satellite orbit and clock	Precision orbit provided by WHU
Antennas phase center offset	Igs14_2196.atx model (Rebischung & Schmid, 2014)
Earth occlusion range	Earth Radius plus 1000 km for atmosphere
Receiver acquisition threshold	15 dB Hz
System noise temperature	Nadir: 175 K, Zenith: 200 K
Observation data rate	PHO:1 s, LTO:3 s
Receiver clock model	Two-state Kalman Filter covariance model (Dierendonck et al., 1987) PSD coefficients: $h_0 = 2.9 \times 10^{-23}$; $h_1 = 4.5 \times 10^{-30}$; $h_2 = 3.4 \times 10^{-31}$ (Iiyama et al., 2021)
Pseudo-range measurement noise	Random errors related to the C/N_0 and Elevation-dependent multipath model (Li et al., 2024)

Wang *et al. Satellite Navigation*   (2024) 5:16

Page 11 of 22

For the BDS B1C signal, the data component is modulated by the sine-phased BOC (1,1), where the pre-correlation band-limiting of the front-end can be neglected. The code tracking noise standard deviation corresponds to that of the BPSK signal multiplied by a factor 1/2 (Groves, 2013).

As we described in the introduction, an accurate 3D antenna model is important for simulations. Therefore, we used the BDS-3 and GPS 3D antenna model to achieve a more accurate simulation. Figures 6 and 7 show the antenna equivalent isotropically radiated power, which includes the power amplifier and transmitting antenna gain. GPS L1 models of all types of satellites were released by Lockheed Martin (Marquis & Reigh, 2015) and the BDS-3 B1C models can be obtained from Lin et al. (2020).

Then we assumed that the spacecraft is equipped with nadir and zenith antennas that can capture GPS and BDS-3 signals. A high-gain antenna is mounted on the
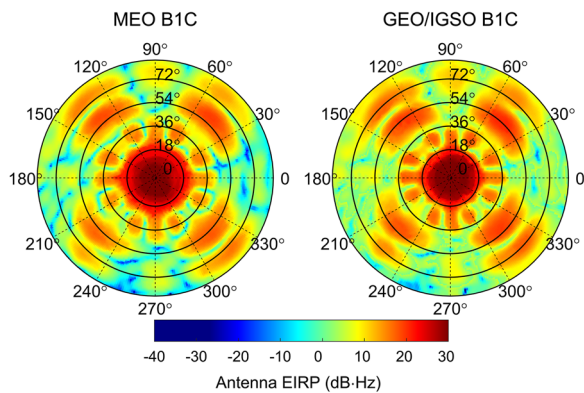

Fig. 8 Receiver antenna gain
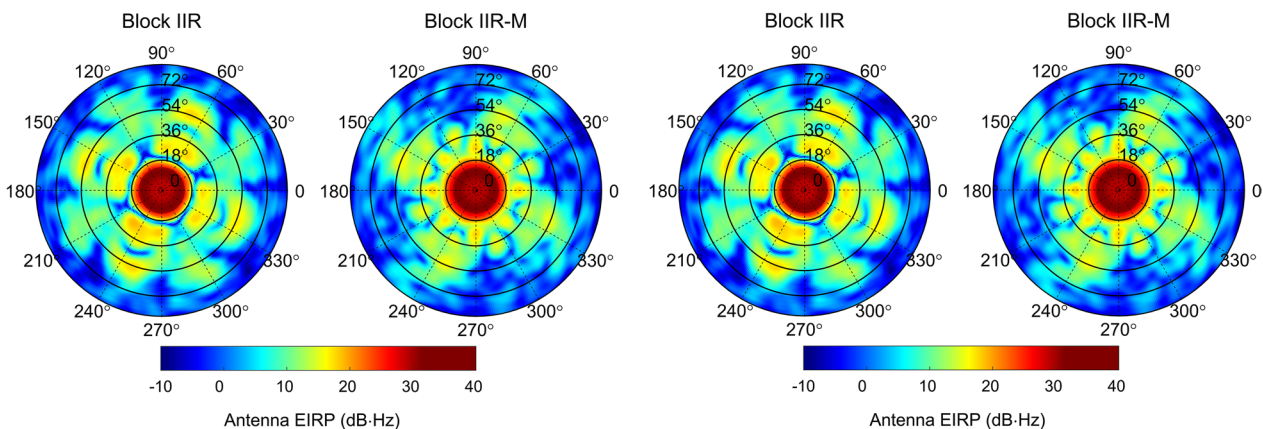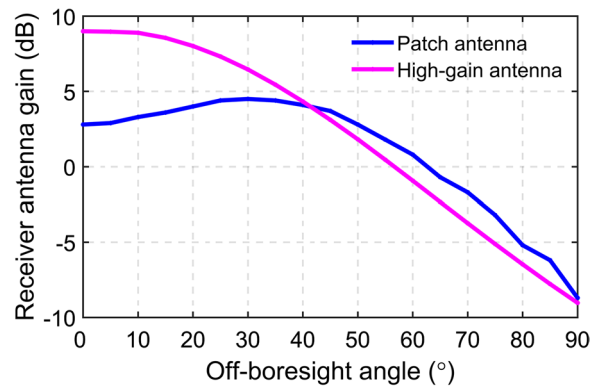
nadir receiver for the weak signals. The receiver antenna gains of the two antennas are shown in Fig. 8. The acquisition and tracking threshold of the receiver adopts the recommended value, which is set to 15 dB Hz (United Nations, 2021).

Now, we can analyze the signal characteristics of GPS and BDS navigation signals received by spacecraft in PHO and LTO. Additionally, we can refer to the calculation method for the Doppler shift (Lin et al., 2020). The two subplots in Fig. 9 show the Doppler shifts (top), C/N_0 (middle), and number of visible satellites (bottom) for PHO and LTO, respectively.

We can determine that, at the beginning of PHO, the main lobe signal Doppler shift variation range can reach ± 50 kHz and is then below ± 15 kHz after 3 h, and the side lobe signal Doppler shift is approximately ± 25 kHz in the entire orbit. Regarding LTO, the main lobe signal has a lower Doppler shift variation range, which is approximately ± 13 kHz, and the side lobe signal is approximately ± 25 kHz. Additionally, we can see that the main lobe received signal C/N_0 is

Fig. 6 BDS antenna pattern for B1C

Fig. 7 GPS antenna pattern for L1
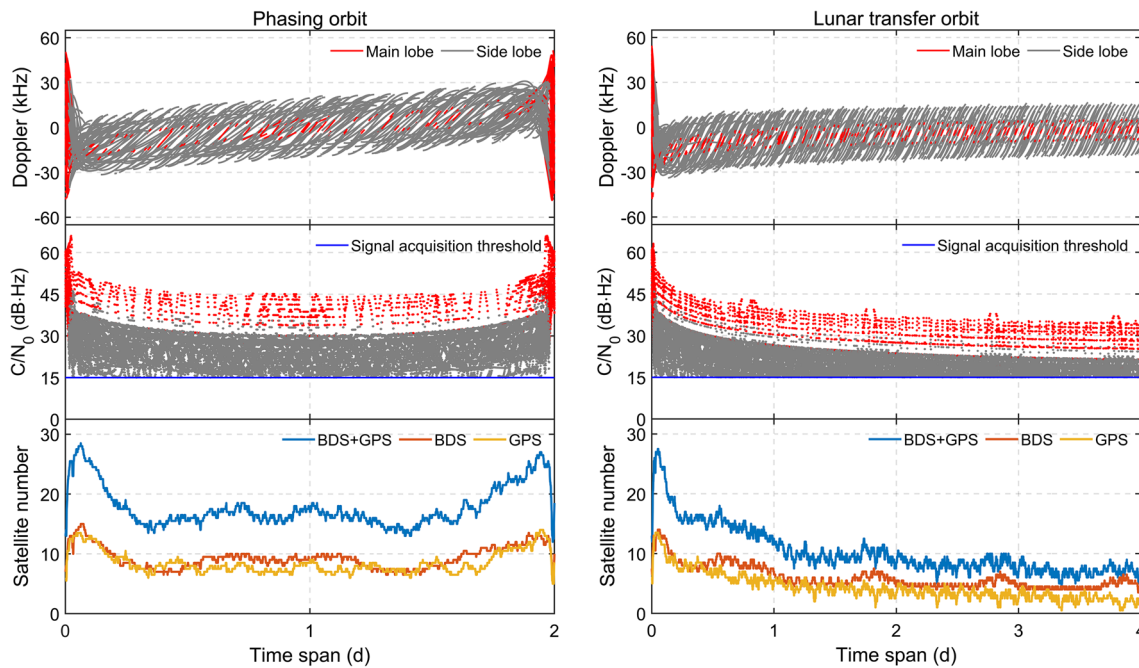
Fig. 9 Doppler shift (top), C/N_0 (middle), and number of visible satellites (bottom) for PHO (left) and LTO (right)

higher than 40 dB·Hz, and even reaches 60 dB Hz and the side lobe is lower than 40 dB Hz in PHO. In LTO, the maximal main lobe received signal C/N_0 can be approximately 35 dB·Hz; while the most side lobe signals are lower than 20 dB·Hz. Additionally, we found that GNSS can provide continuous signals for earth–moon spacecraft, and weak GNSS signals can still be received even near the moon.

According to Eq. (45), the minimum, maximum, and average values of the thermal noise code tracking jitter can be obtained for PHO and LTO, as shown in Fig. 10. We can see that the disparity of the ranging noise of different satellites is large, the maximum value is more than 10 m, and the minimum value is better than 5 m, which is

mainly related to the satellite antenna transmitting power and free space loss.

IMU and star tracker

An aerospace IMU was be used and the parameters of the accelerometer and gyroscope are shown in Tables 5 and 6, respectively (Capuano et al., 2014; Groves, 2013).

Regarding the star tracker, the diagonal field size of the simulated star tracker is set to 10 degrees, the focal length is 85 mm, and the threshold of the stellar magnitude is 7 Mv. Additionally, the Hipparcos catalog is chosen as the navigation catalog (ESA, 1997). Considering the accuracy of the star tracker is mainly affected by the recognition error of starlight in the image coordinate system, we set
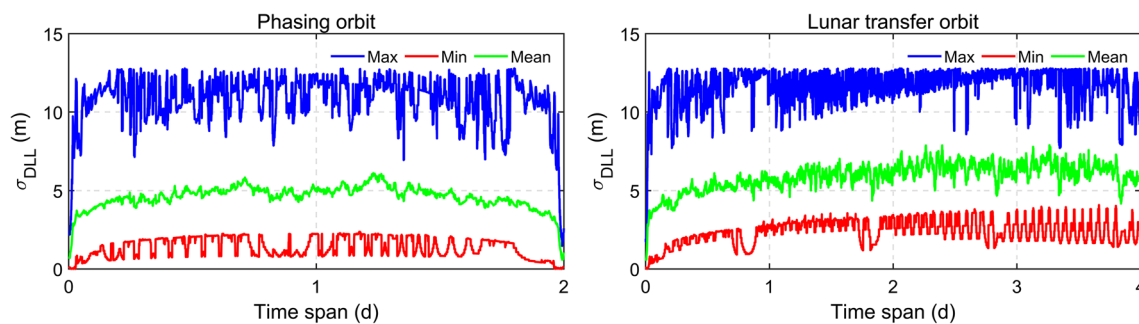
Fig. 10 Maximum (blue), minimum (red), and average (green) of the thermal noise range error of PHO (left) and LTO (right)

Table 5 Accelerometer characteristics

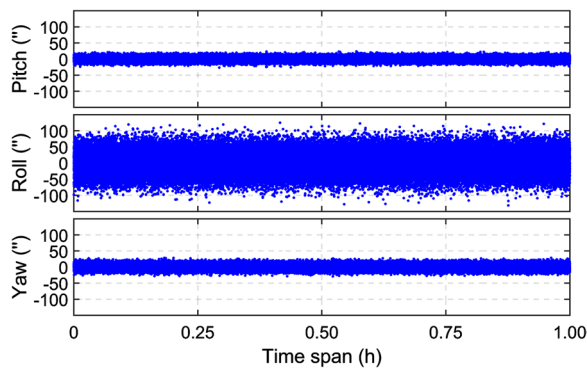| Parameter	Value
Accelerometer biases in x, y, z direction ($G_1 = 9.80665 \times 10^{-6} \text{m/s}^2$)	$\begin{bmatrix} 30 \times G_1 & -45 \times G_1 & 26 \times G_1 \end{bmatrix}$
Accelerometer scale factor and cross coupling errors	$\begin{bmatrix} 100 \times 10^{-6} & -120 \times 10^{-6} & 80 \times 10^{-6} \\ -60 \times 10^{-6} & -120 \times 10^{-6} & 100 \times 10^{-6} \\ -100 \times 10^{-6} & 40 \times 10^{-6} & 90 \times 10^{-6} \end{bmatrix}$
Accelerometer noise root PSD	$20 \times 9.80665 \times 10^{-6} \text{m} \cdot \text{s}^{-2} \cdot \text{Hz}^{-0.5}$
Accelerometer quantization level	$\begin{bmatrix} 5 \times 10^{-5} \text{m/s}^2 \end{bmatrix}$

Table 6 Gyro characteristics

Parameter	Value
Gyro biases ((°)/h)	$\begin{bmatrix} -9 \times 10^{-4} & 13 \times 10^{-4} & -8 \times 10^{-4} \end{bmatrix}$
Gyro scale factor and cross coupling errors	$\begin{bmatrix} 8 \times 10^{-6} & -120 \times 10^{-6} & 100 \times 10^{-6} \\ 0 & -6 \times 10^{-6} & -60 \times 10^{-6} \\ 0 & 0 & -7 \times 10^{-6} \end{bmatrix}$
Gyro noise root PSD ((°)/h)	2×10^{-3}
Accelerometer quantization level (rad/s^2)	$\begin{bmatrix} 1 \times 10^{-6} \end{bmatrix}$

the recognition error to 1×10^{-5} degrees to be as close as possible to the actual error. Figure 11 shows the attitude solution error of the simulated star tracker with a time interval of 1 s. The accuracy of the pitch, roll, and yaw are 3.87, 31.43, and 5.31″, respectively, which is consistent with "Blue Canyon Technologies Nano-Star Tracker" mentioned in Capuano et al. (2014). Additionally, it is worth noting that the accuracy of the roll angle is much lower than that of the pitch and yaw, which is also reasonable (Liebe, 2002).

Experiments and analysis

After we obtained the simulate observations of multi-sensors, the accuracy of orbit determination using multi-sensors can be analyzed this section.

Table 7 Detailed configuration for GNSS gross error

Satellite PRN	The epoch of gross error (s)	Gross error (m)
C24	1200–1400	$\sim N(200, \sigma_{\text{DLL}}^2)$
C25	1300–1500	$\sim N(100, \sigma_{\text{DLL}}^2)$
G17	2000–2100	$\sim N(30, \sigma_{\text{DLL}}^2)$

FDE for GNSS observations

Firstly, in order to maintain the reliability and stability of state solution in low C/N_0 environment, the gross errors

Fig. 11 Attitude determination error of the simulated star tracker
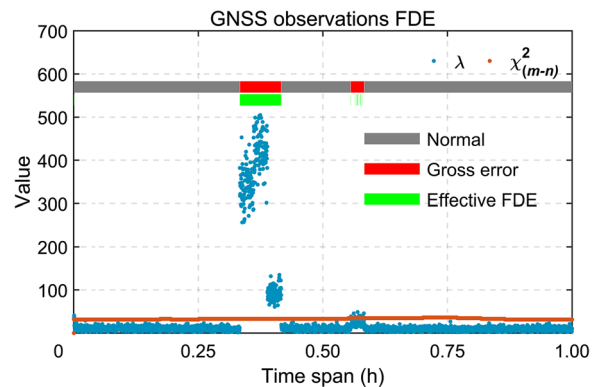
Fig. 12 Value of λ_k and Chi-square distribution threshold in the process of solution and the success rate of elimination is counted

Wang *et al. Satellite Navigation* (2024) 5:16

Page 14 of 22

of GNSS observations must be detected and excluded before state estimation.

The LTO orbit at the 48th hour was selected as the target orbit and the gross errors was added to the observations from three GNSS satellites, with the detailed configuration shown in Table 7.

Then FDE algorithm mentioned above is used to detect and eliminate gross errors, Fig. 12 provides the value of λ_k and Chi-square distribution threshold $\chi^2_{m-n}(\alpha = 0.01)$ in the calculation process.

It can be seen that gross errors of C24 and C25 will cause value of λ_k to increase significantly, which exceeds the corresponding detection threshold and can

be easily detected and excluded, but the detection rate of small gross errors of G17 is significantly reduced by FDE algorithm. The recognition and exclusion rates for C24, C25, and G17 are 100%, 100%, and 30%, respectively. The solution results before and after the FDE algorithm used are shown in Figs. 13 and 14, and the statistical results are presented in Table 8.

Obviously, the gross error in the observations makes the solution result extremely worse, and the accuracy of position and velocity determination is obviously decreased, which reduces the reliability of autonomous navigation using GNSS. However, FDE algorithm can excluded gross errors and the solution results can be maintained in 3-sigma confidence intervals, even if the recognition ability of small gross errors is limited.
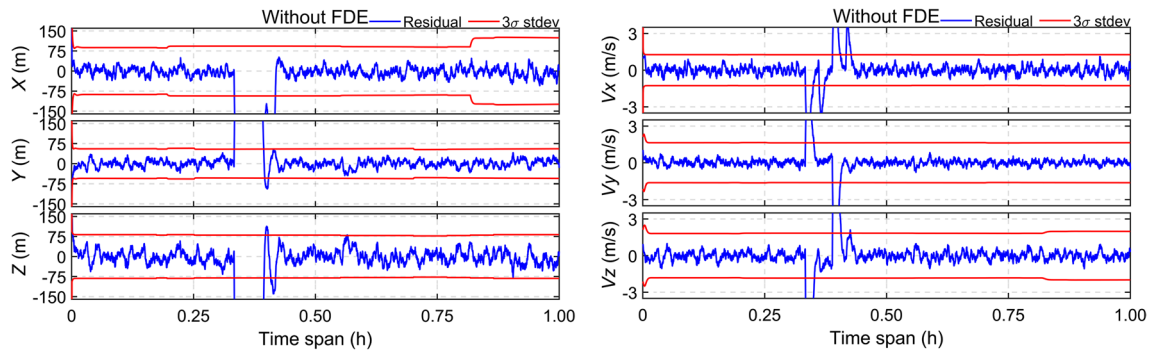
Fig. 13 Results of position (left) and velocity (right) determination without FDE algorithm. (The three direction position result probabilities of being within the 3-sigma are 91.58%, 93.19%, and 94.08%. Additionally, the velocity results are 94.61%, 96.67%, and 96.25%, respectively)
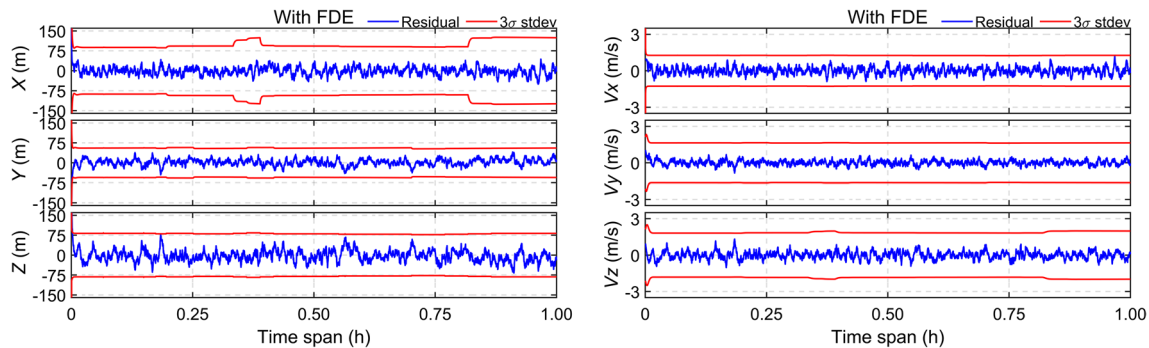
Fig. 14 Results of position (left) and velocity (right) determination without FDE algorithm. (The three direction position result probabilities of being within the 3-sigma are 100.00%, 99.94%, and 100.00%. Additionally, the velocity results in all directions are 100.00%)

Table 8 Statistical values of solution results with and without FDE algorithm

Scheme	Position in different direction (m)			Velocity in different direction (m/s)		
	X	Y	Z	Vx	Vy	Vz
Without FDE	149.52	160.01	290.25	1.82	2.08	3.69
With FDE	15.14	23.81	23.43	0.30	0.21	0.31

Table 9 Parameter settings (*r* is the distance from the Earth's center)

	Item	Setting
Dynamic model	Earth gravity model	$r < 9600$km GGM05S (10×10) 9600km $\leq r < 50000$km GGM05S (6×6) 50000km $< r$ GGM05S (2×2)
	Moon gravity model	particle model
	N-body	JPL DE421 (Folkner et al., 2009)
	Solar radiation pressure	Macro model
	Solid tide and pole tide	IERS 2010
	Ocean tide	FES 2004
	Relatively	IERS 2010
Observation model	Satellite Orbit and clock	Broadcast ephemeris
	Observations	Simulated GNSS observations
	Initial position variance	5 000 m
	Initial velocity variance	2 m/s
	Initial clock bias	1 µs
	Filter Type	Adaptive Kalman filter

Navigation use GNSS with the adaptive algorithm

According to the above analysis, GNSS can provide continuous available signals for spacecraft in earth–moon space, which is suitable for spacecraft navigation. In addition, considering the noise in GNSS observation, the proposed adaptive algorithms are also used in the autonomous navigation solution of the Earth–moon spacecraft.

The dynamic model and observation model parameters for the Kalman filter configuration settings are listed in Table 9. Because of the limited power of the onboard processor unit, and the higher-order gravity term has no significant effect on the accuracy of orbit determination for high and ultra-high orbits. We use gravity models of various orders at different locations in earth–moon space, which significantly reduces the amount of computation while maintaining similar navigation performance.

We design three schemes to evaluate the performance of integrated navigation and the adaptive algorithm proposed in this study:

Scheme 1 (short for S1): Navigation solution based on the Kalman filter with the constant covariance matrix (the diagonal elements of the covariance matrix are set to the constant 10 m for pseudo-range).

Scheme 2 (short for S2): Navigation solution based on the Kalman filter with the MBAE algorithm. (For GPS, we set the coefficients of a and b in Eq. (35) to 0.1596 and 32.0745, respectively. Additionally, for BDS-3, we set the values to 0.0798 and 16.0373, respectively.)

Scheme 3 (short for S3): Navigation solution based on the Kalman filter with the IBAE algorithm.

The solution results for the position and velocity for the three schemes of PHO and are shown in Figs. 15, 16 and 17. Additionally, the statistical Root Mean Square (RMS) of the solutions are listed in Table 10. We can
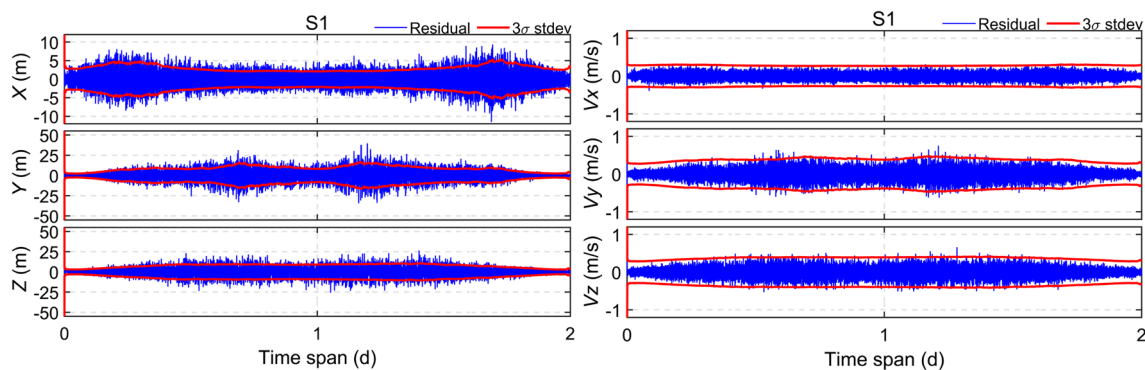
Fig. 15 Results of the PHO position (left) and velocity (right) determination of S1. (The three direction position result probabilities of being within the 3-sigma are 94.95%, 94.65%, and 95.22%. Additionally, the velocity results are 99.97%, 99.72%, and 99.80%, respectively)
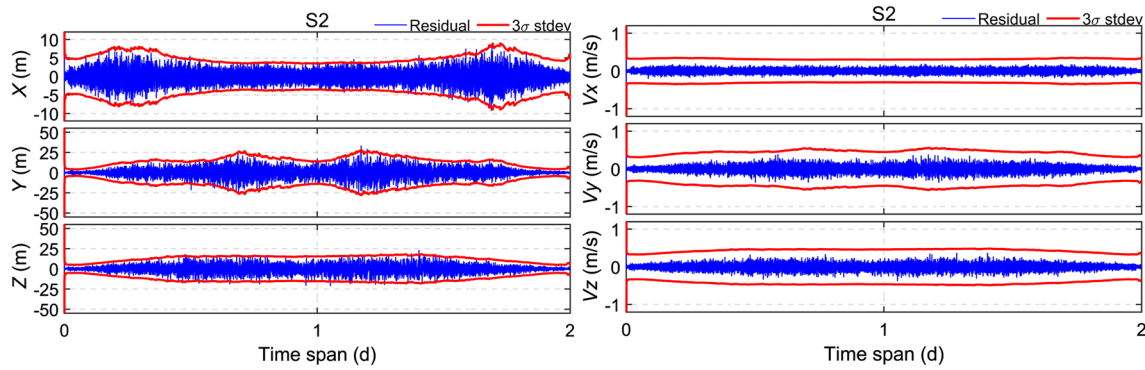
Fig. 16 Results of the PHO position (left) and velocity (right) determination of S2. (The three direction position result probabilities of being within the 3-sigma are 99.94%, 99.94%, and 99.93%. Additionally, the velocity results in all directions are 100.00%)
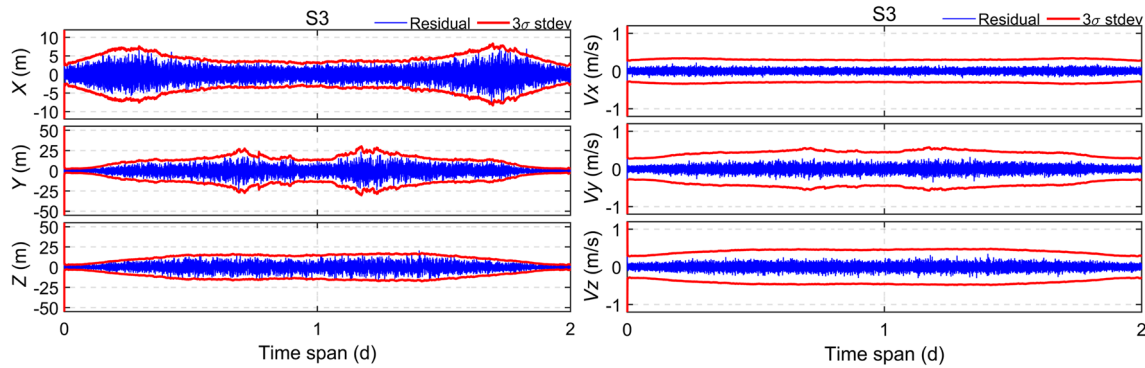
Fig. 17 Results of the PHO position (left) and velocity (right) determination of S3. (The position result probabilities of being within the 3-sigma are 99.97%, 99.98%, and 99.97%. Additionally, the velocity results in all directions are 100.00%)

Table 10 Statistical values of the PHO solution results for the three schemes

| Scheme	Position in different direction (m)			Velocity in different direction (m/s)		
	X	Y	Z	Vx	Vy	Vz
S1	1.89	6.27	5.09	0.08	0.14	0.13
S2	1.58	5.25	4.30	0.05	0.08	0.08
S3	1.37	4.38	3.70	0.05	0.07	0.07

conclude that compared with S1, the position accuracy of S2 increased by 16.0% and the velocity accuracy increased by 38.7%. Additionally, more solutions exist in the 3-sigma range. S3 has the highest solution accuracy and the average position error of the solution is 99.97% within the 3-sigma. Compared with S1, the position and velocity accuracy increased by 28.3% and 44.3%, respectively, which proves the effectiveness of the proposed IBAE algorithm.

Similarly, we used the same three strategies to determine the position and velocity of LTO. Additionally, we statistically calculated the accuracy of the solutions in three segments according to distance r between the spacecraft and the center of the Earth, where $r < 20R_E$, $20R_E < r < 40R_E$, and $40R_E < r < 60R_E$, and R_E is the radius of the Earth. The results are shown in Figs. 18, 19 and 20 and Table 11. Similar to PHO, the navigation performance of S3 is also better than that of S2 and S1. Compared with S1, S3 has a position accuracy increase of 36.27%, the average probability of being within the range of 3-sigma is 99.97%, and the average probability of the velocity result within the range of 3-sigma is 100.00%.
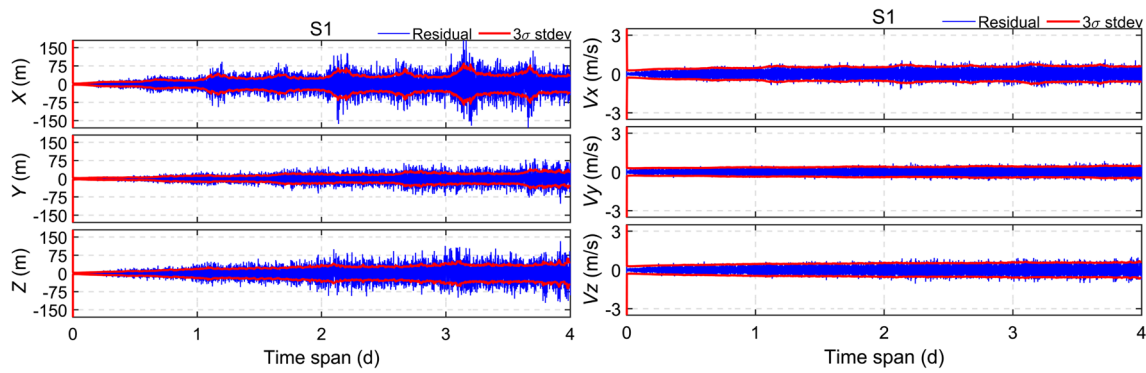
Fig. 18 Results of the LTO position (left) and velocity (right) determination of S1. (The position result probabilities of being within the 3-sigma are 90.92%, 90.84%, and 90.78%. Additionally, the velocity results are 98.85%, 99.13%, and 98.91%, respectively)
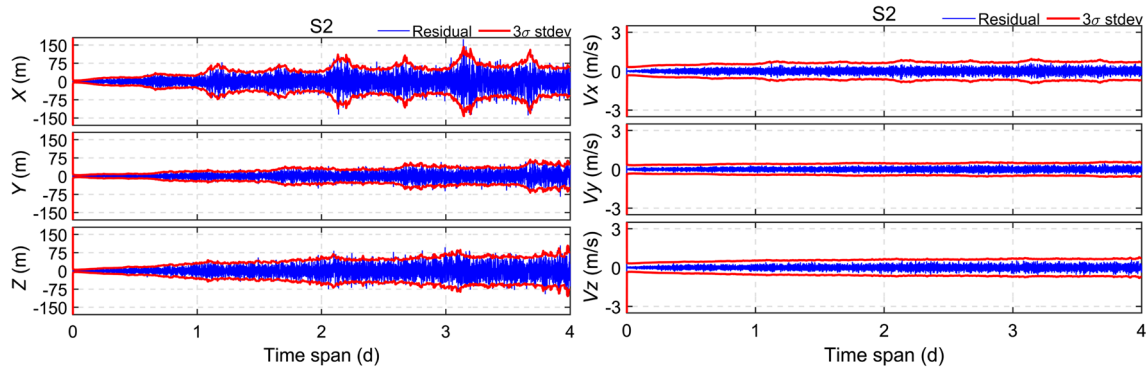
Fig. 19 Results of the LTO position (left) and velocity (right) determination of S2. (The position result probabilities of being within the 3-sigma are 99.56%, 99.57%, and 99.40%. Additionally, the velocity results are 99.99%, 99.99%, and 100.00%, respectively)
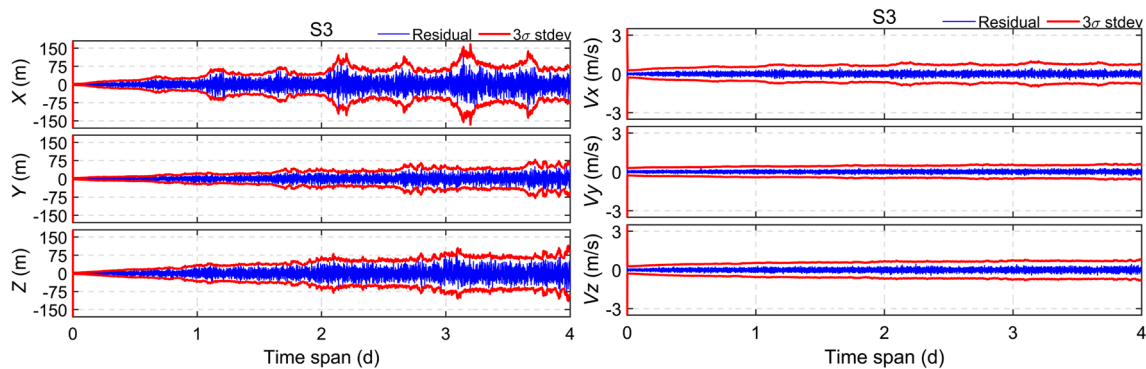

Fig. 20 Results of the LTO position (left) and velocity (right) determination of S2. (The position result probabilities of being within the 3-sigma are 99.56%, 99.57%, and 99.40%. Additionally, the velocity results are 99.99%, 99.99%, and 100.00%, respectively)

Additionally, the left and right figures in Fig. 21 show the position results in PHO and LTO with the C/N_0 thresholds of 15, 20, and 25 dB Hz. And the statistical results of the position accuracy and the number of visible satellites with different C/N_0 threshold are shown in Fig. 22. To analyze the performance of

GNSS in lunar space, only the results at the end of the LTO ($40R_E < r < 60R_E$) were counted. We found that, compared with the navigation performance of spacecraft in PHO, that of spacecraft in LTO is significantly affected by the C/N_0 threshold. If the threshold of C/N_0 increase to 20 dB Hz, the navigation accuracy near lunar

Wang *et al. Satellite Navigation*   (2024) 5:16

Page 18 of 22

Table 11 Statistical values of the LTO solution results for the three schemes

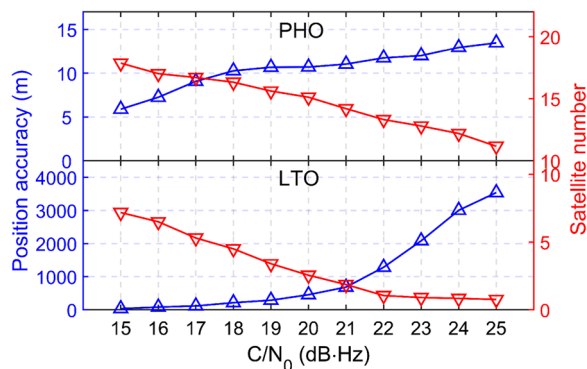| Distance	Scheme	Position in different direction (m)			Velocity in different direction (m/s)		
		X	Y	Z	Vx	Vy	Vz
$r < 20R_E$	S1	12.67	6.10	9.42	0.17	0.12	0.15
	S2	10.72	5.11	7.86	0.10	0.07	0.09
	S3	9.03	4.15	6.43	0.09	0.06	0.08
$20R_E < r < 40R_E$	S1	26.15	13.36	21.10	0.26	0.16	0.23
	S2	21.81	11.19	17.71	0.15	0.10	0.14
	S3	17.75	9.22	14.45	0.12	0.08	0.10
$40R_E < r < 60R_E$	S1	35.15	20.92	30.21	0.30	0.20	0.26
	S2	29.67	17.73	25.73	0.17	0.12	0.16
	S3	22.97	14.27	20.87	0.13	0.09	0.12
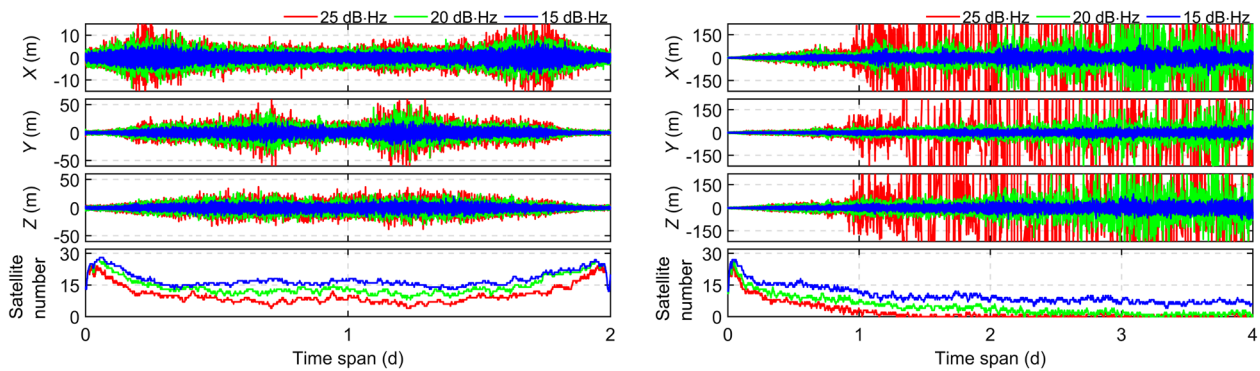
Fig. 21 Navigation performance of spacecraft in PHO (left) and LTO (right) when the C/N_0 thresholds are set to 15, 20, and 25 dB Hz

space deteriorates significantly, and continuous navigation services cannot be achieved if the threshold is set to 25 dB Hz. Therefore, the spacecraft needs to carry a receiver with a C/N_0 threshold of 15 dB Hz to navigate with GNSS in cis-lunar space, which is also a common view. For PHO, the requirement of the C/N_0 threshold is relatively low, and the navigation performance

Fig. 22 Navigation performance in PHO (up) and LTO (down) with various SNR thresholds. (The position accuracy and number of visible satellites are shown in blue and red, respectively)

better than 15 m can be obtained even with a threshold of 0.25 dB Hz.

In conclusion, we found that GNSS can provide navigation services in most regions of earth–moon space through simulation experiments. Additionally, we verified the effectiveness of the proposed adaptive algorithm, which can further improve the performance of the navigation service of GNSS with an accurate dynamic model, and provide a reference for the use of GNSS in earth–moon space. By the way, it can be seen that there are obvious fluctuations in the curves of PHO and LTO solution results, which is caused by GNSS positioning geometry.

Integrated navigation with INS, GNSS and star tracker

During the long-term flight in deep space, the spacecraft will inevitably be disturbed by unknown acceleration that cannot be modeled (e.g., the change of the space environment or orbital maneuver). The accuracy of the dynamics model based on orbital mechanics will be significantly reduced, and the accuracy of the solution will be significantly deteriorated. Spaceborne accelerometers can make
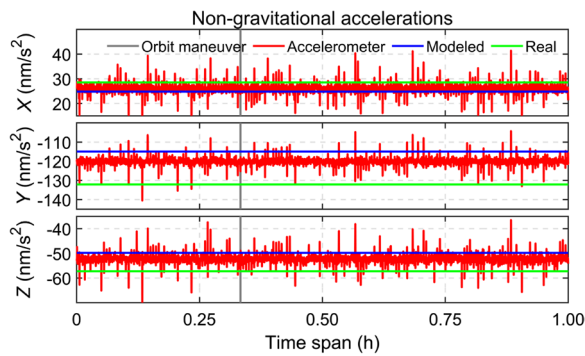
Fig. 23 Assumed real acceleration (green), model acceleration used in the orbital filter (blue), and acceleration measured by the accelerometer (red). Considering the scale limit, the change of the maneuvering acceleration is not displayed

up for the defects of orbital mechanics and provide an accurate dynamic model. We attempt to analyze the navigation accuracy of the dynamic model compensated for

by the accelerometer when the spacecraft is subjected to unknown acceleration.

We assume that the spacecraft made an orbital maneuver in LTO at 15:41:51.907 on April 24, 2007. An acceleration of $(0.281096, -0.194355, 0.0755011)$ m/s^2 was applied in the X, Y, and Z directions in b-frame for 10 s. At this time, the known dynamic model failed and the additional acceleration caused by this orbital maneuver can be obtained by on-board accelerometer. In addition, the moment of using accelerometer data can be determined according to the difference between accelerometer data and model acceleration, since normally the difference should not be significant.

Orbits 20 min before and 40 min after the moment of the maneuver were selected, and the accelerometer data were simulated according to the characteristics of the accelerometer in Table 4. Figure 23 shows the assumed real acceleration of the spacecraft, the model acceleration in the orbit filter, and the simulated accelerometer data.

It should be noted that the premise of using the proposed IBAE algorithm is an accurate dynamic model,
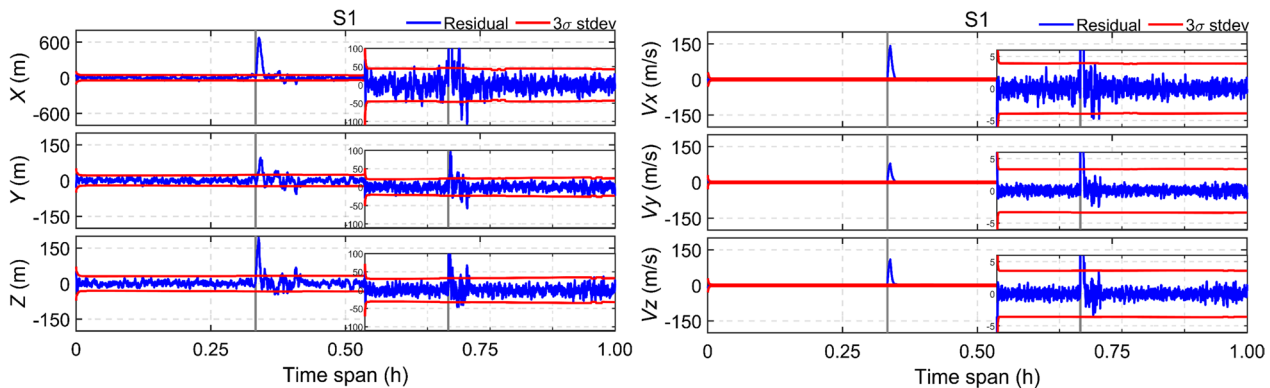
Fig. 24 Position (left) and velocity (right) results of S1. (The position result probabilities of being within the 3-sigma are 96.31%, 96.19%, and 95.89%. Additionally, the velocity results are 99.17%, 99.83%, and 99.44%)
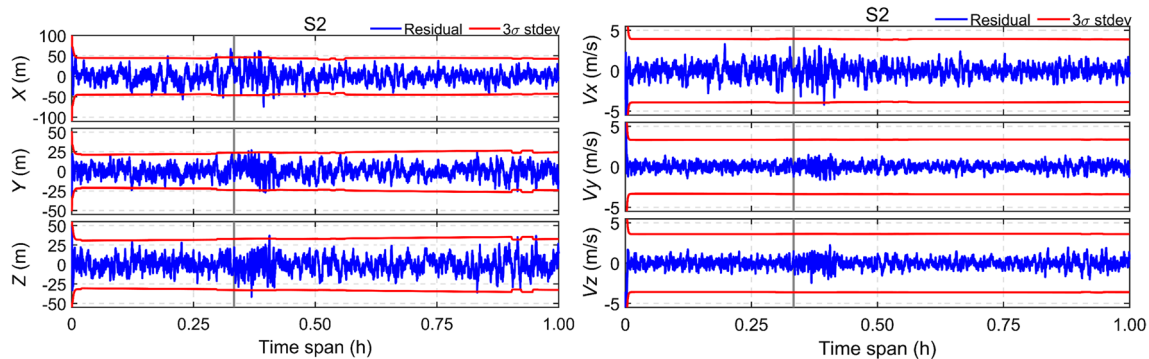

Fig. 25 Position (left) and velocity (right) results of S2. (The position result probabilities of being within the 3-sigma are 99.61%, 99.33%, and 99.56%. Additionally, the velocity results in all directions are 100.00%)

Wang *et al. Satellite Navigation*   (2024) 5:16

Page 20 of 22

Table 12 Statistical results for the two schemes

Scheme	Position in different direction (m)			Velocity in different direction (m/s)		
	X	*Y*	*Z*	*Vx*	*Vy*	*Vz*
S1	55.31	10.90	16.51	9.60	5.22	7.10
S2	16.46	7.99	9.89	0.96	0.57	0.73
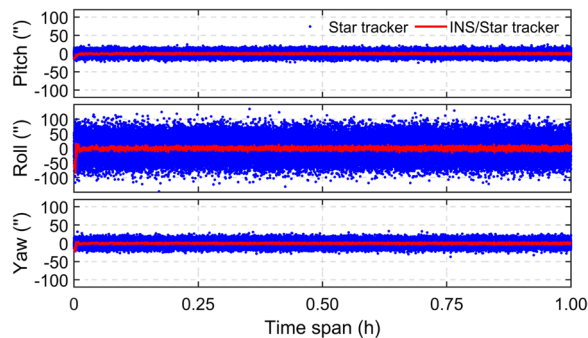
Fig. 26 Attitude solution results determined by a single star tracker and gyro/star tracker integrated system

only the MBAE algorithm can be used when the orbit maneuvers. Two schemes were designed to evaluate the navigation accuracy during the orbital maneuver:

Scheme 1 (short for S1): Navigation solution using GNSS observations based on the Kalman filter.

Scheme 2 (short for S2): Integrated navigation using INS, GNSS, and star tracker during the orbital maneuver.

The results are shown in Figs. 24 and 25, and the RMS values are listed in Table 12. In Fig. 24. We found that relying only on the orbital dynamic model cannot maintain navigation accuracy during the orbital maneuver, and the position and velocity accuracies decrease rapidly, with position accuracy even below 500 m. However, when the accelerometer data are used instead of the dynamic model, navigation accuracy returns to normal.

Additionally, it is considered that the attitude of spacecraft can be determined using a gyroscope and star tracker. The spacecraft attitude determined by the star tracker alone and the gyroscope, star tracker integrated solution is provided in Fig. 26.

We found that the attitude determination accuracy of the single star tracker is better than 50 arcseconds, and the combined solution of the gyroscope and the star tracker can further improve accuracy and is better than 10 arcseconds.

Conclusions and discussion

Considering the need for autonomous navigation for future spacecraft, we explored the navigation performance of GNSS in earth–moon space. And an autonomous navigation system based on the GNSS receiver, IMU, and star tracker integrated system with orbit filtering is adopted. Additionally, we proposed the MBAE and IBAE algorithms, which we used in the case of GNSS ranging accuracy attenuation in earth–moon space.

Signal characteristics received by PHO and LTO orbiting spacecraft were analyzed, which shows that satellite navigation signals can cover most areas in Earth–moon space. The experiment shows that users can receive more BDS satellites than GPS, which may be due to the stronger power of the BDS sidelobe signal, and the higher orbital altitude of the BDS GEO and IGSO.

The accuracies of PHO in the *X*, *Y*, and *Z* directions using GNSS and orbital filter solving are 1.89, 6.27, and 5.09 m, respectively. Accuracy improved by 16.0% with the MBAE algorithm and further improved by 28.3% with the IBAE algorithm. A similar conclusion also be obtained for LTO, where the accuracies are 35.15, 20.92, and 30.21 m in the three directions when the spacecraft distance from the center of the Earth is greater than 40 Re, which proves that GNSS can provide navigation services in near-lunar space. We verified the effectiveness of the proposed adaptive algorithm. Additionally, we considered spacecraft maneuvers, for which position accuracy was substantially reduce than 500 m when determined using GNSS alone with the orbit filter; hence, we used accelerometers to compensate for the dynamic model, and improve the position and velocity accuracy during orbital maneuvers use INS, GNSS and star tracker integration navigation system. With the integration of a gyroscope and star tracker, an attitude accuracy of better than 10 arcseconds can be obtained.

Based on the above experiments and analysis, we proved the feasibility of autonomous navigation using GNSS for Earth–moon spacecraft, and then proposed an adaptive algorithm to effectively suppress GNSS observations noise, so that high-precision position of spacecraft can still be obtained in lunar space. Finally, the performance of INS, GNSS and star tracker integrated navigation system is verified, and the solution accuracy can be maintained during orbital maneuvers.

In the future, we will consider the integration of more sensors and navigation methods (e.g., the celestial

Wang *et al. Satellite Navigation*   (2024) 5:16

Page 21 of 22

navigation system) to further improve the autonomous navigation performance of spacecraft in and outside earth–moon space.

Declarations

Competing interests
Tianhe Xu is an editorial board member for Satellite Navigation and was not involved in the editorial review or decision to publish this article. All authors declare that they have no competing interests.

References
Aghapour, E., & Farrell, J. A. (2019). Outlier Accommodation in sensor rich environments: Moving horizon risk-averse performance-specified state estimation. In *2019 IEEE 58th conference on decision and control (CDC)* (pp. 7917–7922). IEEE.

Bauer, F. H., Parker, J. J. K., Welch, B., & Enderle, W. (2017). *Developing a robust, interoperable GNSS space service volume (SSV) for the global space user community* (pp. 132–149).

Bhaskaran, S., Riedel, J., Synnott, S., & Wang, T. (2000). The deep space 1 autonomous navigation system—A post-flight analysis. In *Astrodynamics specialist conference*. American Institute of Aeronautics and Astronautics.

Brunner, F. K., Hartinger, H., & Troyer, L. (1999). GPS signal diffraction modelling: The stochastic SIGMA-δ model. *Journal of Geodesy, 73*(5), 259–267. https://doi.org/10.1007/s001900050242

Capuano, V., Botteron, C., Wang, Y., Tian, J., Leclère, J., & Farine, P.-A. (2014). *GNSS/INS/Star tracker integrated navigation system for earth-moon transfer orbit* (pp. 1433–1447). ION.

Capuano, V., Opromolla, R., Cuciniello, G., Pesce, V., Sarno, S., Capuano, G., Lavagna, M., Grassi, M., Corraro, F., Tabacco, P., Meta, F., Battagliere, M.L., & Tuozzi, A. (2018). A highly integrated navigation unit for on-orbit servicing missions. In: *International astronautical congress*.

Capuano, V., Shehaj, E., Botteron, C., Blunt, P., & Farine, P.-A. (2017). GNSS/INS/Star tracker integration for real-time on-board autonomous orbit and attitude determination in LEO, MEO, GEO and beyond. In *68th International astronautical congress*.

Delépaut, A., Giordano, P., Ventura-Traveset, J., Blonski, D., Schönfeldt, M., Schoonejans, P., Aziz, S., & Walker, R. (2020). Use of GNSS for lunar missions and plans for lunar in-orbit development. *Advances in Space Research, 66*(12), 2739–2756. https://doi.org/10.1016/j.asr.2020.05.018

Delépaut, A., Schönfeldt, M., Giordano, P., Blonski, D., Sarnadas, R., Ries, L., & Ventura-Traveset, J. (2019). A system study for cislunar radio navigation leveraging the use of realistic Galileo and GPS signals (pp. 1199–1219).

Dierendonck, A. J. V., McGraw, J. B., & Brown, R. G. (1987). Relationship between Allan variances and Kalman filter parameters. In *Proceedings of the sixteenth annual precise time and material interval (PTTI) applications and planning meeting a meeting held at the NASA Goddard space flight center* (pp. 273–293).

Ely, T., Bhaskaran, S., Bradley, N., Lazio, T. J. W., & Martin-Mur, T. (2022). Comparison of deep space navigation using optical imaging, pulsar time-of-arrival tracking, and/or radiometric tracking. *Journal of Astronautical Sciences, 69*(2), 385–472. https://doi.org/10.1007/s40295-021-00290-z

Erhu, W., Yile, L., Yanlin, L., Yidan, H., & Jingnan, L. (2023). Quality analysis of VLBI observation data of Chang'e-4/5 Lunar probe. *Journal of Geodesy and Geodynamics in China*. https://doi.org/10.14075/j.jgg.2023.09.123

ESA. (1997). *The Hipparcos and Tycho Catalogues (ESA SP-1200)*. ESA.

Folkner, W. M., Williams, J. G., & Boggs, D. H. (2009). The planetary and lunar ephemeris DE 421. In *Interplanetary network progress report* (pp. 42–178).

Förste, C., Bruinsma, S. L., Shako, R., Abrikosov, O., Flechtner, F., Dahle, C., Neumeyer, H., Barthelmes, F., Biancale, R., Balmino, G., & König, R. (2012). A new release of EIGEN-6: The latest combined global gravity field model including LAGEOS, GRACE and GOCE data from the collaboration of GFZ Potsdam and GRGS toulouse (geophysical research abstracts Vol. 14, EGU2012-2821-2, 2012). In *Proceedings of the general assembly European geosciences union*.

Gao, B., Hu, G., Gao, S., Zhong, Y., & Gu, C. (2018). Multi-sensor optimal data fusion for INS/GNSS/CNS integration based on unscented Kalman filter. *International Journal of Control, Automation and Systems, 16*(1), 129–140. https://doi.org/10.1007/s12555-016-0801-4

Gao, Y., Krakiwsky, E. J., Abousalem, M. A., & McLellan, J. F. (1993). Comparison and analysis of centralized, decentralized, and federated filters. *Navigation, 40*(1), 69–86. https://doi.org/10.1002/j.2161-4296.1993.tb02295.x

Groves, P. (2013). *Principles of GNSS, inertial, and multisensor integrated navigation systems* (2nd ed.). Artech House.

Guan, M., Xu, T., Li, M., Gao, F., & Mu, D. (2022). Navigation in GEO, HEO, and lunar trajectory using multi-GNSS sidelobe signals. *Remote Sensing, 14*(2), 318. https://doi.org/10.3390/rs14020318

Gui, M., Xi, N., Ma, X., & Ye, W. (2021). A fast star angle/time delay measurement integrated navigation method. *Journal of Deep Space Exploration, 8*(2), 190–197.

Hewitson, S., & Wang, J. (2007). GNSS receiver autonomous integrity monitoring with a dynamic model. *Journal of Navigation, 60*(2), 247–263. https://doi.org/10.1017/S0373463307004134

Hu, G., Xu, L., Gao, B., Chang, L., & Zhong, Y. (2023). Robust unscented Kalman filter-based decentralized multisensor information fusion for INS/GNSS/CNS integration in hypersonic vehicle navigation. *IEEE Transactions on Instrumentation and Measurement, 72*, 1–11. https://doi.org/10.1109/TIM.2023.3281565

Iiyama, K., Kawabata, Y., & Funase, R. (2021). *Autonomous and decentralized orbit determination and clock offset estimation of lunar navigation satellites using GPS signals and inter-satellite ranging* (pp. 936–949).

International Space Exploration Coordination Group. (2018). *The global exploration roadmap 2018*. NASA.

International Space Exploration Coordination Group. (2022). *The global exploration roadmap 2022*. CSA.

Jiang, C., Zhang, S., Cao, Y., Li, H., & Zheng, H. (2020). A robust fault detection algorithm for the GNSS/INS integrated navigation systems. *Journal of Geodesy and Geoinformation Science, 3*(1), 12–24.

Konopliv, A. S., Park, R. S., Yuan, D., Asmar, S. W., Watkins, M. M., Williams, J. G., Fahnestock, E., Kruizinga, G., Paik, M., Strekalov, D., Harvey, N., Smith, D. E., & Zuber, M. T. (2013). The JPL lunar gravity field to spherical harmonic degree 660 from the GRAIL primary mission. *JGR Planets, 118*(7), 1415–1434. https://doi.org/10.1002/jgre.20097

Li, D., Dan, P., He, B., Chen, Y., Zhang, Y., & Shi, P. (2022a). Satellite integrated navigation method based on starlight angular distance/laser ranging. *Chinese Space Science and Technology, 42*(3), 67–73.

Li, M., Wei, K., Xu, T., Shi, Y., & Wang, D. (2024). Enhanced precise orbit determination for GPS and BDS-2/3 with real LEO onboard and ground observations. *Measurement, 224*, 113912. https://doi.org/10.1016/j.measurement.2023.113912

Li, M., Xu, T., Shi, Y., Wei, K., Fei, X., & Wang, D. (2022b). Adaptive Kalman filter for real-time precise orbit determination of low earth orbit satellites based on pseudorange and epoch-differenced carrier-phase measurements. *Remote Sensing, 14*(9), 2273. https://doi.org/10.3390/rs14092273

Wang *et al. Satellite Navigation* (2024) 5:16

Page 22 of 22

Liebe, C. C. (2002). Accuracy performance of star trackers—A tutorial. *IEEE Transactions on Aerospace and Electronic Systems, 38*(2), 587–599. https://doi.org/10.1109/TAES.2002.1008988

Lin, K., Zhan, X., & Huang, J. (2019). GNSS signals ionospheric propagation characteristics in space service volume. *International Journal of Space Science and Engineering, 5*(3), 223–241. https://doi.org/10.1504/IJSPACESE.2019.101404

Lin, K., Zhan, X., Yang, R., Shao, F., & Huang, J. (2020). BDS space service volume characterizations considering side-lobe signals and 3D antenna pattern. *Aerospace Science and Technology, 106*, 106071. https://doi.org/10.1016/j.ast.2020.106071

Liu, Q., Huang, Y., Shu, F., Wang, G., Zhang, J., Chen, Z., Li, P., Ma, M., & Hong, X. (2022). VLBI technique for the orbit determination of Tianwen-1. *Sci Sin-Phys Mech Astron, 52*(3), 239507. https://doi.org/10.1360/SSPMA-2021-0204

Lopes, H. D., Silva, J. S., Silva, P. F., Musumeci, L., Dovis, F., Serant, D., Calmettes, T., Challamel, R., Ospina, J. A., Pessina, I., & Perello, J. V. (2014). *GNSS-based navigation for lunar missions*. Tampa Convention Center.

Lyard, F., Lefevre, F., Letellier, T., & Francis, O. (2006). Modelling the global ocean tides: Modern insights from FES2004. *Ocean Dynamics, 56*(5–6), 394–415. https://doi.org/10.1007/s10236-006-0086-x

Ma, X., Dong, X., & Hu, Y. (2023). Analysis on navigation accuracy of high orbit spacecraft based on BDS GEO and IGSO satellites. *Advances in Space Research, 71*(5), 2481–2492. https://doi.org/10.1016/j.asr.2022.10.040

Marquis, W. A., & Reigh, D. L. (2015). The GPS block IIR and IIR-M broadcast L-band antenna panel: Its pattern and performance—GPS block IIR and IIR-M L-band antenna panel pattern. *NAVIGATION: Journal of the Institute of Navigation, 62*(4), 329–347. https://doi.org/10.1002/navi.123

Montenbruck, O., & Gill, E. (2012). *Satellite orbits: Models, methods*. Springer-Verlag.

Ning, X., Wang, L., Wu, W., & Fang, J. (2011). A celestial assisted INS initialization method for lunar explorers. *Sensors, 11*(7), 6991–7003. https://doi.org/10.3390/s110706991

Petit, G., & Luzum, B. (2010). IERS conventions 2010; No.36 in IERS Technical Note. IERS Conventions Centre.

Qi, D. C., Oguri, K. (2023). Investigation on autonomous orbit determination in Cislunar space via GNSS and horizon-based measurements.

Rathinam, A., & Dempster, A. G. (2016). *Multi-GNSS for space service volume*. Colombo Theatres, Kensington Campus, UNSW Australia.

Rebischung, P., & Schmid, R. (2014). IGS14/igs14.atx: A new framework for the IGS products.

Shehaj, E., Capuano, V., Botteron, C., Blunt, P., & Farine, P.-A. (2017). GPS based navigation performance analysis within and beyond the space service volume for different transmitters' antenna patterns. *Aerospace, 4*(3), 44. https://doi.org/10.3390/aerospace4030044

Sirbu, G., & Leonardi, M. (2023). Fully autonomous orbit determination and synchronization for satellite navigation and communication systems in halo orbits. *Remote Sensing, 15*(5), 1173. https://doi.org/10.3390/rs15051173

Teunissen, P. J. G. (1998). Quality control and GPS. In P. J. G. Teunissen & A. Kleusberg (Eds.), *GPS for geodesy* (pp. 271–318). Springer.

Ulvestad, J. S. (1992). Use of the VLBI delay observable for orbit determination of earth-orbiting VLBi satellites. *TDA Progress Report Jet Propulsion Laboratory Pasadena*, 42–110.

United Nations. (2021). *The interoperable global navigation satellite systems space service volume*. UN.

Wang, P., & Zhang, Y. (2013). New method of satellite autonomous navigation based on accelerometer and celestial navigation. *Journal of Chinese Inertial Technology, 21*(4), 489–523. https://doi.org/10.13695/j.cnki.12-1222/o3.2013.04.021

Wei, C., Shao, K., Gu, D., Zhang, Z., Zhu, J., An, Z., & Wang, J. (2023). Enhanced orbit and baseline determination for formation-flying LEO satellites with spaceborne accelerometer measurements. *Journal of Geodesy, 97*(7), 64. https://doi.org/10.1007/s00190-023-01753-x

Yang, Y., Gao, W., & Zhang, X. (2010). Robust Kalman filtering with constraints: A case study for integrated navigation. *Journal of Geodesy, 84*(6), 373–381. https://doi.org/10.1007/s00190-010-0374-6

Yu, P., Zhang, H., Li, J., Guan, Y., Wang, L., Zhao, Y., Chen, Y., Yang, W., Yu, J., Wang, H., Wang, Z., Wang, Z., Wang, L., Zhang, X., Chen, S., Hu, H., & Xu, J. (2021). Design and implementation of GNC system of lander and ascender module of Change-5 spacecraft. *SCIENTIA SINICA Technologica, 51*(7), 763–777. https://doi.org/10.1360/SST-2021-0104

Publisher's Note